

## **Small Airway Reduction and Fibrosis is an Early Pathologic Feature of Idiopathic Pulmonary Fibrosis**

Kohei Ikezoe<sup>1</sup>, Tillie-Louise Hackett<sup>1</sup>, Samuel Peterson<sup>2</sup>, Dante Prins<sup>1</sup>, Cameron J. Hague<sup>3</sup>, Darra Murphy<sup>3</sup>, Stacey LeDoux<sup>1</sup>, Fanny Chu<sup>1</sup>, Feng Xu<sup>1</sup>, Joel D. Cooper<sup>4</sup>, Naoya Tanabe<sup>5</sup>, Christopher J. Ryerson<sup>1</sup>, Peter D. Paré<sup>1</sup>, Harvey O. Coxson<sup>1</sup>, Thomas V. Colby<sup>6</sup>, James C. Hogg<sup>1</sup>, and Dragoş M. Vasilescu<sup>1</sup>

<sup>1</sup>Centre for Heart and Lung Innovation, St. Paul's Hospital, University of British Columbia, Vancouver, BC, Canada.

<sup>2</sup>VIDA Diagnostics, Coralville, IA, USA.

<sup>3</sup>Department of Radiology, University of British Columbia, Vancouver, BC, Canada.

<sup>4</sup>Department of Thoracic Surgery, University of Pennsylvania. Philadelphia, PA, USA.

<sup>5</sup>Department of Respiratory Medicine, Graduate School of Medicine, Kyoto University, Kyoto.

<sup>6</sup>Department of Laboratory Medicine and Pathology, Mayo Clinic, Scottsdale, AZ, USA.

**Running title:** Small airways disease in IPF

**Author Contributions:** KI, TLH, SP, DP, CJH, DM, SL, FC, FX, JDC, TVC and DMV contributed to data collection. KI, TLH, DP, NT, CJR, PDP, HOC, JCH, DMV contributed to study design, data interpretation, figures and writing. All authors read and approved the manuscript.

**Grants:** K. Ikezoe is supported by MSD life Science Foundation, Public interest Incorporated Foundation Fellowship. D. M. Vasilescu is supported by the Parker B. Francis Foundation Fellowship and a Canadian Lung Association Grant. T.-L. Hackett is supported by a Canadian

Institutes of Health Research (CIHR) and Michael Smith Foundation for Health Research New Investigator Awards and is a Tier I Canada Research Chair in asthma and COPD pathobiology & therapeutics. The study was, in part, funded through investigator-initiated grants from the British Columbia Lung Association and CIHR.

Correspondence and requests for reprints should be addressed to Dragoş M. Vasilescu, Ph.D., B.Sc., UBC Centre for Heart Lung Innovation, St. Paul's Hospital, Rm 166, 1081 Burrard Street, Vancouver, B.C. V6Z 1Y6 Canada. E-mail: [Dragos.Vasilescu@hli.ubc.ca](mailto:Dragos.Vasilescu@hli.ubc.ca).

This article has an online data supplement, which is accessible from this issue's table of content online at [www.atsjournals.org](http://www.atsjournals.org)

## **At a Glance Commentary**

### **Scientific Knowledge on the subject**

To date, studies on the pathology of idiopathic pulmonary fibrosis (IPF) have primarily focused on the histopathological hallmarks of the disease: subpleural fibrosis, subepithelial fibroblast foci, and microscopic honeycombing. The recent use of ultra-high resolution micro-computed tomography has greatly improved our understanding of the complex lung structure and how it is remodeled in IPF. However, there is limited information on the morphology of early IPF lesions, which are vital to understanding disease pathology.

### **What this study adds to the field**

Stereological assessment of the pathology of end-stage IPF lungs compared to age-matched controls using multi-resolution 3D imaging demonstrates that the smallest airways within the lung, the conducting terminal bronchioles and respiratory transitional bronchioles, are reduced in

number, and the terminal bronchiolar walls are thickened, in regions of the lung that have no microscopic fibrosis. Further, this study demonstrates that in regions of microscopic fibrosis in IPF lungs, the remaining terminal bronchioles have thicker airway walls and the airway lumen becomes distorted and dilated leading to the formation of honeycomb cysts. The data presented in this study have important implications for the current thinking on how the lung tissue is remodeled in IPF and highlights small airways as a potential target to modify IPF outcomes.

**ABSTRACT (Words 248)**

**Rationale:** To improve disease outcomes in idiopathic pulmonary fibrosis (IPF) it is essential to understand its early pathophysiology so that it can be targeted therapeutically.

**Objectives:** Perform three-dimensional (3D) assessment of the IPF lung micro-structure using stereology and multi-resolution computed tomography (CT) imaging.

**Methods:** Explanted lungs from IPF patients (n=8) and donor controls (n=8) were inflated with air and frozen. CT scans were used to assess large airways. Unbiased, systematic uniform random (SUR) samples (n=8/lung) were scanned with microCT for stereological assessment of small airways (number, airway wall and lumen area) and parenchymal fibrosis (volume fraction of tissue, alveolar surface area, and septal wall thickness).

**Results:** The total number of airways on clinical CT was greater in IPF lungs than control lungs ( $p<0.01$ ), due to an increase in the wall ( $p<0.05$ ) and lumen area ( $p<0.05$ ) resulting in more visible airways with a lumen larger than 2 mm. In IPF tissue samples without microscopic fibrosis, assessed by the volume fraction of tissue using microCT, there was a reduction in the number of the terminal ( $p<0.01$ ) and transitional ( $p<0.001$ ) bronchioles, and an increase in terminal bronchiole wall area ( $p<0.001$ ) compared to control lungs. In IPF tissue samples with microscopic parenchymal fibrosis, terminal bronchioles had increased airway wall thickness ( $p<0.05$ ), and dilated airway lumens ( $p<0.001$ ) leading to honeycomb cyst formations.

**Conclusion:** This study has important implications for the current thinking on how the lung tissue is remodeled in IPF, and highlights small airways as a potential target to modify IPF outcomes.

## INTRODUCTION

Idiopathic Pulmonary Fibrosis (IPF) is a chronic progressive fibrosing interstitial lung disease (ILD) of unknown cause that primarily affects older adults. Despite two recently approved anti-fibrotic therapeutic agents(1–3), IPF remains a devastating disease with a median time of survival from diagnosis of only three to five years(4, 5). The histopathological hallmarks of the disease are subpleural fibrosis, subepithelial fibroblast foci, and microscopic honeycombing(6–9). To improve the disease outcomes in IPF, it is essential to understand the pathophysiology of the disease so that the early lesions can be targeted therapeutically. However, there is limited information on the morphology of early lesions within IPF lungs.

Multi-detector computed tomography (MDCT) plays a central role in the clinical diagnosis of IPF because of its non-invasive nature(10). However, despite the advances in MDCT diagnosis, histopathological confirmation is still required in many cases to make a definitive diagnosis(4, 10). Recent studies employing ultra-high resolution microCT imaging have bridged the gap in resolution between MDCT and histopathology. These studies have provided new insights into the three-dimensional (3D) pathology of IPF, demonstrating: 1) the non-connectivity of fibroblastic foci(6), 2) the reduction of terminal bronchioles (last generation of conducting airways) in regions of lung tissue scored by a radiologist as minimal and established fibrosis on MDCT(11), and 3) the association between the reduction of terminal bronchioles and the formation of honeycomb cysts(12).

The goal of this study was to obtain new insights into the microscopic structural changes that occur within the IPF lung, by using stereology to assess the relationship of small airway remodeling to microscopic tissue fibrosis quantified on microCT by the volume fraction of tissue. Importantly, by using an unbiased, systematic uniform random (SUR) sampling design of

whole lungs, we were able to assess the heterogeneity of disease lesions in lungs from end-stage IPF patients compared to matched, donor-control lungs. The study demonstrates that a reduction in small airways and airway wall fibrosis in IPF can be found in regions of lung tissue without microscopic parenchymal fibrosis. However, when the surrounding tissue contains microscopic fibrosis, the small airways become dilated and distorted leading to the formation of honeycomb cysts. These volumetric data have important implications for the current thinking on how the lung tissue is remodeled in IPF, and the potential of targeting small airway reduction to modify outcomes in patients with IPF. Some of the results in this study have been previously reported in the form of abstracts(13, 14).

## **METHODS**

### **Subjects**

Single explanted lungs from 8 patients with end-stage IPF following bilateral lung transplantation and 8 unused donor control lungs, matched for age and sex were obtained at the University of Pennsylvania Hospital (Philadelphia, PA, USA), with the approval of the University of Pennsylvania Hospital Institutional Review Board. Informed consent was obtained from the patients or the donor's next of kin. The study was conducted and approved by the University of British Columbia Research Ethics Board (#H07-0021). Subject demographics, pulmonary function and MDCT data are provided in Table 1. The diagnosis of IPF was made through multidisciplinary discussions following current diagnostic guidelines(4). For this study, the MDCT scans and histopathology were re-evaluated by independent radiologists (CJH and DM) and pathologist (TVC), see Table E1.

### **3D-imaging-based stereology**

The study workflow is shown in Figure 1, with procedures described in detail elsewhere(15–17). Briefly, pre-operative MDCT scans were performed for all IPF patients before lung transplantation (parameters: 100-120kV, 67-270mA, 0.625-2.5mm slice thickness).

Lung tissue samples were taken using a previously described SUR sampling method(17–19). Briefly, lungs were inflated with air, frozen, and imaged with MDCT (parameters, 120kV, 178mA, 0.625mm slice thickness). The specimen MDCT scans were used to obtain: total lung volume, mean CT attenuation value, %tissue volume, %air space volume, total airway count, cross-sectional airway wall area and airway lumen area(17, 20). The frozen lungs were sliced from apex to base, and eight SUR tissue samples per lung (23x23mm) were taken.

**MicroCT:** Tissue samples were maintained frozen ( $-30^{\circ}\text{C}$ ) using a cryo-stage during microCT (parameters: 50kV, 350 $\mu\text{A}$ , molybdenum target, 354ms exposure time, gain 24dB) as previously described(16, 17). Images were acquired at two isotropic resolutions: 13 $\mu\text{m}$  for airway analysis and 7 $\mu\text{m}$  for parenchymal analysis.

**Stereology:** A detailed description of the stereology methods are provided in the online supplement (Figure E1-E9). All quantitative image analysis was performed in ImageJ(21). Terminal (TBs) and transitional bronchioles (TrBs) were defined, counted and segmented as previously described(22, 23). The centerlines of terminal bronchioles were used to generate exact cross-sectional images which enabled the computation of the following parameters: wall area, coefficient of variation of wall thickness, lumen area and roundness, branch roughness and curviness as previously described(17). Lung parenchyma was separated into aerated and non-aerated tissue(24), and point counts for each tissue type were used to determine the respective volume fractions. Line intercepts were used to calculate mean airspace chord length, alveolar surface density, alveolar surface area, and septal wall thickness as previously described(17, 19).

Following microCT scanning, tissue samples were formalin-fixed and paraffin-embedded. Tissue sections were stained using hematoxylin and eosin for histopathological diagnosis.

### **Statistical analysis**

A Shapiro-Wilk normality test was used to assess the distribution of the data. The demographic data were compared using a non-paired T-test and reported as mean $\pm$ [SD]. To compare all parameters between control and IPF cases a non-parametric Mann–Whitney U test was used. For comparison between three groups, a likelihood ratio test was performed to compare the models with and without the grouping variable, and Tukey’s post hoc test for multiple comparisons. A linear mixed-effect model was used to investigate the difference between IPF and control samples, with the subject identifier as a random effect. All statistical analyses were performed using the statistical software R version 4.0.2(25). A p-value  $<0.05$  was considered statistically significant.

## **RESULTS**

### **Demographic and quantitative MDCT comparisons**

Demographic, physiological features and MDCT data for the IPF patients and donor controls are shown in Table 1. The IPF cases had a reduced forced expiratory volume in 1 second (FEV<sub>1</sub>), forced vital capacity (FVC), but a preserved FEV<sub>1</sub>/FVC ratio compared to the calculated values derived from the demographic data of the control subjects(26). As shown in Table E1, three IPF patients were assigned a radiologic pattern consistent with an alternative diagnosis, but all of the IPF cases had a pathological pattern of usual interstitial pneumonia (UIP) that supported a diagnosis of IPF. The quantitative analysis of the specimen MDCT scans showed that the IPF lungs had a smaller total lung volume ( $p<0.01$ ) and % airspace volume ( $p<0.01$ ), which



coincided with a higher mean CT attenuation value ( $p<0.01$ ) and % tissue volume ( $p<0.01$ ) compared to control lungs (Table 1).

### **Comparison of large and small airway features between control and IPF lungs**

Figure 2A and B are representative images from an IPF and a control lung for: 1) a slice from the specimen MDCT scan showing the location of a SUR tissue sample taken from that slice (red circle), 2) the reconstructed MDCT airway tree, 3) a representative microCT slice for the SUR tissue sample taken, 4) the reconstructed airway tree from the microCT, and 5) a terminal bronchiole viewed in cross-section.

The total visible airway count derived from the specimen MDCT scans was greater in IPF lungs ( $561\pm315$ ) compared to control lungs ( $196\pm113$ ,  $p<0.01$ , Figure 2C). As shown in Figure 2D, the number of airways visible on the MDCT scans was increased in airway generations 7-17 in IPF lungs compared to control lungs ( $p<0.05$ ). Airway wall area ( $\text{mm}^2$ ) was greater in airway generations 10-13 in IPF patients compared to control subjects ( $p<0.05$ , Figure 2E). Airway lumen area ( $\text{mm}^2$ ) was greater in airway generations 12-13 in IPF lungs compared to control lungs ( $p<0.05$ , Figure 2F). In IPF lungs, airways from generation 14-17 had comparable airway wall thickening and lumen dilatation as airway generations 12-13, but no airways in generations 14-17 were visible in control lungs for statistical comparison.

From the analysis of small airways using microCT, it was found that the total number of both terminal (Figure 2G,  $p<0.001$ ) and transitional (Figure 2H,  $p<0.001$ ) bronchioles per lung were reduced in IPF patients compared to controls. The wall area (Figure 2K,  $p<0.001$ ) and variance in the wall thickness (Figure 2L,  $p<0.01$ ) of terminal bronchioles was greater in IPF lungs compared to control lungs. The lumen area of terminal bronchioles in IPF lungs was

increased (Figure 2M,  $p<0.01$ ) and they were less round (Figure 2N,  $p<0.05$ ) compared to control lungs. As visualized in the 3D-reconstruction of the microCT airway tree (Figure 2B), terminal bronchioles were distorted over their entire branch length with localized dilatations in IPF lungs, quantified by greater values for branch roughness (Figure 2J,  $p<0.001$ ) and curviness (Figure 2I,  $p<0.05$ ) compared to control lungs.

### **Comparison of parenchymal features between control and IPF lungs**

The microCT images in Figure 3 show the heterogeneity of microscopic lung fibrosis in different lung tissue samples taken from an IPF lung (Figure 3A) compared to a control lung (Figure 3B). In IPF lungs, there was an increase in the volume fraction of total parenchymal tissue compared to control lungs (Figure 3C,  $p<0.001$ ). In the IPF lung parenchyma, 81% was aerated and 19% was non-aerated parenchyma, in contrast to controls lungs which contained no non-aerated parenchyma (Figure 3D,  $p<0.001$ ). In the regions of aerated parenchyma, the mean airspace chord length (Figure 3E) was not different between groups, but there was a substantial decrease in the alveolar surface area (Figure 3F,  $p<0.001$ ) in IPF lungs compared to control lungs. The reduction of alveolar surface area in IPF lungs was due to a reduction in the volume fraction of alveolar space (Figure 3G,  $p<0.001$ ), an increase in the volume fraction of septal tissue (Figure 3H,  $p<0.001$ ), and no change in the volume fraction of alveolar ducts (Figure 3I). The increase in the volume fraction of septal tissue was related to an increase in the average septal wall thickness in IPF lungs compared to control lungs (Figure 3J,  $p<0.001$ ). All stereological parameters assessed in the manuscript are provided by case for the IPF lungs in Table E2 and the control lungs in Table E3.

### **Association of small airway remodeling with microscopic fibrosis**

Figure 4A and B show the number of terminal and transitional bronchioles plotted against the volume fraction of tissue as measured on microCT for every control and IPF tissue sample. The upper limit for the volume fraction of tissue in controls (dashed line) was used to define a threshold for samples with and without microscopic tissue fibrosis. In IPF tissue samples with and without microscopic fibrosis, there was a reduction in the number of the terminal (Figure 4C,  $p < 0.01$  and  $p < 0.05$ , respectively) and transitional (Figure 4D,  $p < 0.001$  and  $p < 0.05$ , respectively) bronchioles compared to control samples. The wall area of terminal bronchioles (Figure 4E) was increased in IPF tissue samples with ( $p < 0.001$ ) and without ( $p < 0.05$ ) microscopic fibrosis compared to controls. IPF tissue samples with fibrosis also had a larger wall area compared to IPF tissue samples without fibrosis ( $p < 0.05$ ). Terminal bronchiole branch roughness, which is an indicator of airway lumen distortion and dilatation (Figure 4F), was significantly increased in IPF tissue samples with fibrosis compared to IPF tissue samples without fibrosis ( $p < 0.001$ ) and control samples ( $p < 0.001$ ). These data indicate that in IPF lungs, the lumen of the terminal bronchioles only become dilated and the airway wall further thickened when the surrounding parenchyma becomes fibrotic. To visualize the relationship between microscopic parenchymal fibrosis and the dilation of terminal bronchioles, axial images of a microCT scan of IPF tissue samples without (Figure 4G) and with parenchymal fibrosis (Figure 4H) are provided. Compared to the IPF sample without fibrosis, the microCT image of the IPF sample with fibrosis shows typical features of honeycomb cysts (orange arrowheads, Figure 4H). The 3D renderings of the small airway structures overlaid onto the axial view of the microCT images demonstrate that in the samples with microscopic fibrosis the honeycomb cysts are in fact part of the conducting airways, which are distorted and dilated by the surrounding parenchymal fibrosis (Figure 4J), compared to samples with no parenchymal fibrosis (Figure 4I).

Clinically, tissue fibrosis can be quantified by an increase in the mean CT attenuation value on MDCT. Figure 5 shows a positive correlation between the mean CT attenuation value for the regions within the IPF lung MDCT scans where tissue samples were taken, and the increase in terminal bronchiole wall area (Figure 5A, standardized beta=0.73,  $p<0.001$ ), lumen area (Figure 5B, standardized beta=0.38,  $p<0.01$ ) and the distortion of the lumen defined as branch roughness (Figure 5C, standardized beta=0.67,  $p<0.001$ ) measured using microCT. There was also a positive correlation between the regional mean CT attenuation values on the IPF lung MDCT scans with the volume fraction of tissue (Figure 5D, standardized beta=0.91,  $p<0.001$ ), septal wall thickness (Figure 5E, standardized beta=0.72,  $p<0.001$ ), and a negative correlation with alveolar surface density (Figure 5F, standardized beta=-0.50,  $p<0.001$ ) measured using microCT.

## DISCUSSION

This study demonstrates that the numbers of conducting terminal bronchioles and respiratory transitional bronchioles are significantly reduced and that the terminal bronchiole airway walls are significantly thickened in regions of the lung that have no microscopic fibrosis in patients with end-stage IPF compared to age-matched controls. Further, this study demonstrates that in regions of microscopic fibrosis in IPF lungs, the remaining terminal bronchioles have thicker airway walls and the airway lumen becomes distorted and dilated leading to the formation of honeycomb cysts. This study highlights that a reduction and fibrosis of small airways in IPF likely occurs early in the disease process as these features are present before microscopic parenchymal fibrosis occurs. This finding highlights the potential importance of the small airways for modification of disease outcomes in IPF.

An earlier report on end-stage IPF lungs, using microCT and a targeted sampling approach, demonstrated that the number of terminal bronchioles is reduced in regions of minimally or established fibrosis that were scored by a radiologist on clinical MDCT scans.

The current study, using a new cohort of IPF and control lungs, supports and extends the previous work, by using an unbiased uniform random sampling design (SURs) to quantify the total number of terminal and transitional bronchioles, airway dimensions, and volume fractions of parenchymal tissues per lung. Importantly, using this stereological analysis of the microanatomy (only visible using histology or microCT (7 - 13  $\mu\text{m}$ )), these data show a reduction in the number of terminal and transitional bronchioles occurs in regions of no “microscopic” fibrosis. The current study also demonstrates that in regions of microscopic fibrosis in IPF lungs, the remaining terminal bronchioles have thicker airway walls and the airway lumen becomes distorted and dilated forming honeycomb cysts. In support of our findings of thickened small airway walls in IPF, Figueira de Mello et al., have recently shown using histology on lung biopsies that small airways (<6mm in diameter) have a greater wall area in UIP and nonspecific interstitial pneumonia patients compared to controls(27). In contrast to our data, these authors reported a narrower airway lumen area for these airways compared to donor controls. This discrepancy may be methodologic. An important aspect of studying the lung structure at any resolution and with any modality is the correct SUR sampling approach as detailed by the ATS/ERS guidelines to obtain unbiased, representative samples of the whole lung(18). Knudsen et al., have recently reviewed the advantages of 3D imaging for stereological studies and concluded that high-resolution microCT 3D imaging has significant advantages over 2D histological studies(28). In the current study, the ability to visualize the entire branch length of the terminal and transitional bronchioles on microCT, and larger conducting airways using

MDCT, revealed that conducting airways in the lungs of IPF patients have marked heterogeneous lumen distortion, dilation and wall thickening along their path length. This heterogeneity in the internal diameter of airways thus confounds the use of airway size to compare similar airway generations in 2D histological studies in IPF.

This study demonstrates that the conducting airway tree in end-stage IPF is remodeled from the 7<sup>th</sup> to the last generation (terminal bronchioles) with thickened walls and dilated lumens, resulting in an increased number of visible airways on MDCT compared to donor controls. These data confirm the previous findings of Verleden et al, in a separate cohort of lungs, who reported increased numbers of airways from the 8<sup>th</sup> – 14<sup>th</sup> generation on MDCT in IPF lungs(11). The authors hypothesized that the increase in the number of visible airways on MDCT was due to airway wall thickening. It is important to note that with the resolution of MDCT (~0.5-1.0mm), airways smaller than 2mm are very difficult to quantify consistently. In this study, we quantified on MDCT that the conducting airway tree in IPF lungs is thickened and dilated along its path length, resulting in more visible airways due to a lumen larger than 2 mm. Further, at the resolution of microCT (13  $\mu$ m), we found the smallest generation of conducting airways, the terminal bronchioles, were thickened and dilated, but also reduced in number. Thus if the resolution of MDCT was such that it could enable us to visualize all conducting airways we would see that the absolute number of conducting airways must be reduced in IPF.

Irregular bronchial dilatation within or around areas of parenchymal abnormality has previously been described as traction bronchiectasis / bronchiolectasis, and this radiological term is used in the current IPF diagnosis guidelines(4, 29–31). However, no measurements of force have been measured to demonstrate that traction induced by the surrounding fibrotic parenchyma is the mechanism for dilation and distortion of the conducting airways. In bronchiolitis obliterans

syndrome and COPD, the small airways have also been shown to be reduced, and the remaining terminal bronchioles thickened, and the airway lumens narrowed and / or occluded(32, 33). In IPF lungs we observed the opposite, the remaining terminal bronchioles have thickened walls, but the airway lumen is distorted and dilated when surrounded by fibrotic parenchymal tissue. These data indicate that traction by the fibrotic parenchyma may indeed be the mechanism for this alteration in airway structure in IPF. Future studies, with the use of precision-cut-lung-slices or other technologies, will be needed to determine if the traction of the fibrotic parenchymal tissue is indeed the mechanism for dilation of the conducting airways in IPF.

Importantly, the 3D visualization of the path length of terminal bronchioles demonstrated that in regions of microscopic fibrosis, thickened and dilated terminal bronchioles form honeycomb cysts. This novel finding may help to explain why honeycomb lesions on 2D histological sections are described as abnormally dilated airspaces with walls composed of fibrotic tissue, lined by an epithelium that shares characteristics with the airway epithelium(34, 35). In support of this finding, Club cells are the dominant airway epithelial cell present within the terminal bronchioles. Recent single-cell RNA sequencing data have identified two unique Club cell sub-populations expressing SCGB3A2 (a Club cell gene) or MUC5B (a known genetic risk factor of IPF), that are increased in the parenchymal tissue of IPF patients and associated with extracellular matrix formation, or production of mucin and immune cell chemoattractants, respectively(36–40). Future studies, combining single-cell sequencing with single-cell spatial imaging technologies, will be essential to understand the structural environment where Club cells reside, if their numbers are increased due to dilation of the terminal bronchiole lumen, and how they contribute to the pathogenesis of IPF. The anatomical data presented in this study, therefore, provide support to a previous hypothesis by Piciucchi et al. that proposed traction bronchiectasis

of conducting airways and honeycombing is a continuum of airway disease throughout the airway tree, rather than separate pathological processes in IPF(41). Together, these observations may also explain why previous IPF studies show that traction bronchiectasis in the large conducting airways correlates with honeycombing on MDCT(42, 43).

It is well understood that the mechanical properties of the lung parenchyma and airways are interdependent(44). The lung parenchyma contains elastic fibers that act radially on the airways while the airways contain longitudinal elastic fibers. When the lung is inflated, the transpulmonary pressure spreads uniformly in alveoli and parenchymal airways and acts on these fibers to increase the length and diameter of the airways. From the 3D analysis of terminal bronchioles in this study, we propose that parenchymal fibrosis results in the significant mechanical distention and dilatation of terminal bronchioles resulting in traction bronchiolectasis, leading to a 320% increase in luminal cross-sectional area. Since the resistance of the tracheobronchial tree is a reflection of the combined resistances of all generations of airways arranged in series and parallel, the large increase in airway lumen size beyond 7<sup>th</sup> generation airways may contribute, along with increased elastic recoil, to the relatively preserved or often increased FEV<sub>1</sub> / FVC ratio due to a disproportionate reduction in FVC compared to FEV<sub>1</sub>(33). In support of this hypothesis, the patients with end-stage IPF in this study had a comparable reduction of terminal bronchioles (81%) to that previously reported in end-stage COPD patients (70%)(33), however the IPF patients had a FEV<sub>1</sub>/FVC ratio of 80%, versus the end-stage COPD patients with an FEV<sub>1</sub>/FVC of 35%. Further, the total cross-sectional area of all remaining terminal bronchioles was calculated per lung. In this study, control lungs had a total terminal bronchiole cross-sectional area of 2299 mm<sup>2</sup> per lung, compared to 1310 mm<sup>2</sup> per lung in IPF lungs, and 934 mm<sup>2</sup> per lung in end-stage COPD (recalculated from previously published



data(33)). These data highlight the effect on FEV<sub>1</sub> with terminal bronchiole reduction and dilatation in IPF, versus terminal bronchiole reduction and obstruction in COPD.

The application of stereology enabled the detailed assessment of both aerated and non-aerated parenchyma in IPF lungs. In regions of aerated parenchyma in IPF lungs, there was a substantial decrease in the alveolar surface area due to the reduction of alveolar air spaces and increased septal wall thickness, with no change in the alveolar duct space or mean airspace chord length. These findings are supported by a much earlier study using stereology on histological sections, which reported a decrease in alveolar surface area and thickening of septal walls in regions defined as “normal” in the lungs of end-stage IPF patients compared to controls(45). Previous reports have shown that the mean CT attenuation of the whole lung is associated with the severity of pulmonary function impairment in IPF patients(46–48). Using image registration on the specimen MDCT, we found the mean CT attenuation for the region of the tissue sample was strongly correlated with parenchymal fibrosis (volume fraction of parenchymal tissue) and terminal bronchiole wall thickening and lumen distortion quantified using microCT. In support of this finding, Miller et al. recently demonstrated that Pi10 (the average wall thickness of a hypothetical airway of 10mm perimeter) was significantly greater in both patients with interstitial lung abnormalities and IPF(49). These studies highlight that radiologic features on MDCT have the potential to be used as an imaging biomarker for early changes in small airways and lung parenchyma. Lung texture analysis has been used to assess radiologic parenchyma features to predict disease outcomes in IPF(50–52). In such studies, it will be important to validate whether existing quantitative MDCT biomarkers using texture analysis or parametric response mapping(53, 54) or novel biomarkers, do correlate with the micro-structure of IPF lesions using microCT. In particular, for many of the radiological features used in the diagnosis

of IPF such as ground-glass opacities and reticulation (thought to be active sites of tissue inflammation and remodeling), it is still unclear what tissue pathologies cause these radiological features. Quantitative studies combining MDCT, microCT and histology will help determine the tissue pathologies associated with each of the radiological features used to diagnose different ILD diseases. In the future, there is also the potential that the resolution of MDCT will improve to assess the small airways and parenchyma *in vivo*, so that individuals with underlying genetic risk factors and/or high-risk family histories may be screened early for disease.

Some limitations should be noted in the present study. First, the eight IPF patients analyzed in this study is small. However, a number of the findings in this study are consistent with those in a previous independent cohort of nine end-stage IPF patients(11). Second, while the availability of whole lungs enabled consistent inflation and unbiased SUR sampling of the lung for stereological assessment, such samples can only be obtained from end-stage IPF patients following lung transplantation. Current biopsy strategies for sampling the peripheral lung or central airways in patients with mild IPF do not allow for such morphometric investigation. However, whole inflated lungs do provide the opportunity to assess the heterogeneous nature of disease pathology, with the assumption that fibrotic lesions represent advanced disease. An additional limitation of such a retrospective cohort study is that it does not allow investigation of disease progression, including whether patients with IPF were born with abnormal lung microstructures and a reduced number of airways. However, recent data on a cross-section cohort of control donor lungs with no smoking history or COPD have shown that the small airways are reduced with ageing after the age of 25 years(55), which supports the notion that small airways can be reduced even further as part of the pathobiology of lung diseases such as COPD and IPF. Third, lung function data was not available for the donor control lungs and could

only be imputed using the donor demographics. Forth, only three control subjects had a smoking history compared to six patients in the IPF group.

In conclusion, stereological assessment of IPF lung pathology using multi-resolution 3D imaging demonstrates that a reduction in small airway number and airway wall fibrosis in IPF likely occurs early in the disease process. Further, terminal bronchioles undergo traction bronchiolectasis resulting in the formation of honeycomb cysts only in the presence of microscopic parenchymal fibrosis. The pathology data presented in this study have important implications for the current thinking on how the lung tissue is remodeled in IPF and highlights the potential of targeting small airway reduction to modify outcomes in patients with IPF.

## **Acknowledgements**

We acknowledge James Latham from the radiology Department at St. Paul's Hospital for performing MDCT scans of whole lungs. Dr. Aaron Barlow from the Cellular Imaging and Biophysics Core for his help with micro-CT image acquisition, Darren Sutherland from the James Hogg Lung Registry for his help with sample preparation, and Chen Xi Yang for assisting in choosing the appropriate statistical methods, all from the UBC Centre for Heart Lung Innovation.

## References

1. King Jr. TE, Bradford WZ, Castro-Bernardini S, Fagan EA, Glaspole I, Glassberg MK, Gorina E, Hopkins PM, Kardatzke D, Lancaster L, Lederer DJ, Nathan SD, Pereira CA, Sahn SA, Sussman R, Swigris JJ, Noble PW, Group AS. A phase 3 trial of pirfenidone in patients with idiopathic pulmonary fibrosis. *N Engl J Med*, 2014/05/20. 2014;370:2083–2092.
2. Richeldi L, du Bois RM, Raghu G, Azuma A, Brown KK, Costabel U, Cottin V, Flaherty KR, Hansell DM, Inoue Y, Kim DS, Kolb M, Nicholson AG, Noble PW, Selman M, Taniguchi H, Brun M, Le Maulf F, Girard M, Stowasser S, Schlenker-Herceg R, Disse B, Collard HR. Efficacy and Safety of Nintedanib in Idiopathic Pulmonary Fibrosis. *N Engl J Med* 2014;doi:10.1056/nejmoa1402584.
3. Hughes G, Toellner H, Morris H, Leonard C, Chaudhuri N. Real World Experiences: Pirfenidone and Nintedanib are Effective and Well Tolerated Treatments for Idiopathic Pulmonary Fibrosis. *J Clin Med* 2016;5:78.
4. Raghu G, Remy-Jardin M, Myers JL, Richeldi L, Ryerson CJ, Lederer DJ, Behr J, Cottin V, Danoff SK, Morell F, Flaherty KR, Wells A, Martinez FJ, Azuma A, Bice TJ, Bouros D, Brown KK, Collard HR, Duggal A, Galvin L, Inoue Y, Jenkins RG, Johkoh T, Kazerooni EA, Kitaichi M, Knight SL, Mansour G, Nicholson AG, Pipavath SNJ, *et al*. Diagnosis of Idiopathic Pulmonary Fibrosis. An Official ATS/ERS/JRS/ALAT Clinical Practice Guideline. *Am J Respir Crit Care Med*, 2018/09/01. 2018;198:e44–e68.
5. Strongman H, Kausar I, Maher TM. Incidence, Prevalence, and Survival of Patients with Idiopathic Pulmonary Fibrosis in the UK. *Adv Ther* 2018;doi:10.1007/s12325-018-0693-1.

6. Jones MG, Fabre A, Schneider P, Cinetto F, Sgalla G, Mavrogordato M, Jogai S, Alzetani A, Marshall BG, O'Reilly KM, Warner JA, Lackie PM, Davies DE, Hansell DM, Nicholson AG, Sinclair I, Brown KK, Richeldi L. Three-dimensional characterization of fibroblast foci in idiopathic pulmonary fibrosis. *JCI Insight*, 2016/06/09. 2016;1(5):e86375.
7. King Jr. TE, Pardo A, Selman M. Idiopathic pulmonary fibrosis. *Lancet*, 2011/07/02. 2011;378:1949–1961.
8. Liebow AA. Definition and Classification of Interstitial Pneumonias in Human Pathology1. *Prog Respir Res* 1975;1–33.doi:10.1159/000398285.
9. Wolters PJ, Collard HR, Jones KD. Pathogenesis of idiopathic pulmonary fibrosis. *Annu Rev Pathol*, 2013/09/21. 2014;9:157–179.
10. Lynch DA, Sverzellati N, Travis WD, Brown KK, Colby T V., Galvin JR, Goldin JG, Hansell DM, Inoue Y, Johkoh T, Nicholson AG, Knight SL, Raoof S, Richeldi L, Ryerson CJ, Ryu JH, Wells AU. Diagnostic criteria for idiopathic pulmonary fibrosis: a Fleischner Society White Paper. *Lancet Respir Med* 2018;doi:10.1016/S2213-2600(17)30433-2.
11. Verleden SE, Tanabe N, McDonough JE, Vasilescu DM, Xu F, Wuyts WA, Piloni D, De Sadeleer L, Willems S, Mai C, Hostens J, Cooper JD, Verbeken EK, Verschakelen J, Galban CJ, Van Raemdonck DE, Colby T V, Decramer M, Verleden GM, Kaminski N, Hackett TL, Vanaudenaerde BM, Hogg JC. Small airways pathology in idiopathic pulmonary fibrosis: a retrospective cohort study. *Lancet Respir Med* 2020;doi:10.1016/S2213-2600(19)30356-X.
12. Tanabe N, McDonough JE, Vasilescu DM, Ikezoe K, Verleden SE, Xu F, Wuyts WA,

- Vanaudenaerde BM, Colby T V, Hogg JC. Pathology of Idiopathic Pulmonary Fibrosis Assessed by a Combination of Microcomputed Tomography, Histology, and Immunohistochemistry. *Am J Pathol* 2020;doi:10.1016/j.ajpath.2020.09.001.
13. Ikezoe K, Vasilescu DM, Hague CJ, Tanabe N, Xu F, Coxson HO, Hogg JC. Quantitative Multi-Resolution Computed Tomography Measures of Lung Parenchyma and Airway Morphometry in Patients with Interstitial Lung Disease. *Am Thorac Soc Int Conf Meet Abstr Am Thorac Soc Int Conf Meet Abstr* American Thoracic Society; 2019. p. A2563–A2563.doi:10.1164/ajrccm-conference.2019.199.1\_meetingabstracts.a2563.
  14. Ikezoe K, Coxson HO, Hague CJ, Peterson S, Cooper JD, Tanabe N, Xu F, Hogg JC, Vasilescu DM. Assessment of Small Airway Morphology Using Micro-Computed Tomography in Patients with Interstitial Lung Disease. *ATS 2020 Int Conf Am Thorac Soc Int Conf Meet Abstr* American Thoracic Society; 2020. p. A4511–A4511.doi:10.1164/ajrccm-conference.2020.201.1\_meetingabstracts.a4511.
  15. McDonough JE, Yuan R, Suzuki M, Seyednejad N, Elliott WM, Sanchez PG, Wright AC, Geftter WB, Litzky L, Coxson HO, Pare PD, Sin DD, Pierce RA, Woods JC, McWilliams AM, Mayo JR, Lam SC, Cooper JD, Hogg JC. Small-airway obstruction and emphysema in chronic obstructive pulmonary disease. *N Engl J Med*, 2011/10/28. 2011;365:1567–1575.
  16. Vasilescu DM, Phillion AB, Tanabe N, Kinose D, Paige DF, Kantrowitz JJ, Liu G, Liu H, Fishbane N, Verleden SE, Vanaudenaerde BM, Lenburg M, Stevenson CS, Spira A, Cooper JD, Hackett TL, Hogg JC. Nondestructive cryomicro-CT imaging enables structural and molecular analysis of human lung tissue. *J Appl Physiol*, 2016/11/20.

- 2017;122:161–169.
17. Vasilescu DM, Phillion AB, Kinose D, Verleden SE, Vanaudenaerde BM, Verleden GM, Van Raemdonck D, Stevenson CS, Hague CJ, Han MK, Cooper JD, Hackett TL, Hogg JC. Comprehensive stereological assessment of the human lung using multiresolution computed tomography. *J Appl Physiol* 2020;128:1604–1616.
  18. Hsia CC, Hyde DM, Ochs M, Weibel ER, Structure AEJTF on QA of L. An official research policy statement of the American Thoracic Society/European Respiratory Society: standards for quantitative assessment of lung structure. *Am J Respir Crit Care Med*, 2010/02/05. 2010;181:394–418.
  19. Vasilescu DM, Klinge C, Knudsen L, Yin L, Wang G, Weibel ER, Ochs M, Hoffman EA. Stereological assessment of mouse lung parenchyma via nondestructive, multiscale micro-CT imaging validated by light microscopic histology. *J Appl Physiol*, 2012/12/25. 2013;114:716–724.
  20. Kirby M, Tanabe N, Tan WC, Zhou G, Obeidat M, Hague CJ, Leipsic J, Bourbeau J, Sin DD, Hogg JC, Coxson HO, Can CCRG, Canadian Respiratory Research N, CanCold Collaborative Research Group the CRRN. Total Airway Count on Computed Tomography and the Risk of Chronic Obstructive Pulmonary Disease Progression. Findings from a Population-based Study. *Am J Respir Crit Care Med* 2018;197:56–65.
  21. Schindelin J, Arganda-Carreras I, Frise E, Kaynig V, Longair M, Pietzsch T, Preibisch S, Rueden C, Saalfeld S, Schmid B, Tinevez JY, White DJ, Hartenstein V, Eliceiri K, Tomancak P, Cardona A. Fiji: an open-source platform for biological-image analysis. *Nat Methods*, 2012/06/30. 2012;9:676–682.



22. Haefeli-Bleuer B, Weibel ER. Morphometry of the human pulmonary acinus. *Anat Rec*, 1988/04/01. 1988;220:401–414.
23. Tanabe N, Vasilescu DM, McDonough JE, Kinose D, Suzuki M, Cooper JD, Pare PD, Hogg JC. Micro-Computed Tomography Comparison of Preterminal Bronchioles in Centrilobular and Panlobular Emphysema. *Am J Respir Crit Care Med*, 2016/09/10. 2017;195:630–638.
24. Lutz D, Gazdhar A, Lopez-Rodriguez E, Ruppert C, Mahavadi P, Günther A, Klepetko W, Bates JH, Smith B, Geiser T, Ochs M, Knudsen L. Alveolar derecruitment and collapse induration as crucial mechanisms in lung injury and fibrosis. *Am J Respir Cell Mol Biol* 2015;52:232–243.
25. R Core Team. R: A Language and Environment for Statistical Computing. 2020;at <<https://www.r-project.org/>>.
26. Quanjer PH, Stanojevic S, Cole TJ, Baur X, Hall GL, Culver BH, Enright PL, Hankinson JL, Ip MSM, Zheng J, Stocks J, Schindler C. Multi-ethnic reference values for spirometry for the 3-95-yr age range: The global lung function 2012 equations. *Eur Respir J* 2012;40:1324–1343.
27. Figueira de Mello GC, Ribeiro Carvalho CR, Adib Kairalla R, Nascimento Saldiva PH, Fernezlian S, Ferraz Silva LF, Dolhnikoff M, Mauad T. Small airway remodeling in idiopathic interstitial pneumonias: a pathological study. *Respiration* 2010;79:322–332.
28. Knudsen L, Brandenberger C, Ochs M. Stereology as the 3D tool to quantitate lung architecture. *Histochem Cell Biol* 2020;doi:10.1007/s00418-020-01927-0.

29. Walsh SLF, Sverzellati N, Devaraj A, Keir GJ, Wells AU, Hansell DM. Connective tissue disease related fibrotic lung disease: High resolution computed tomographic and pulmonary function indices as prognostic determinants. *Thorax* 2014;69:216–222.
30. Edey AJ, Devaraj AA, Barker RP, Nicholson AG, Wells AU, Hansell DM. Fibrotic idiopathic interstitial pneumonias: HRCT findings that predict mortality. *Eur Radiol* 2011;21:1586–1593.
31. Sumikawa H, Johkoh T, Colby T V., Ichikado K, Suga M, Taniguchi H, Kondoh Y, Ogura T, Arakawa H, Fujimoto K, Inoue A, Mihara N, Honda O, Tomiyama N, Nakamura H, Müller NL. Computed tomography findings in pathological usual interstitial pneumonia: Relationship to survival. *Am J Respir Crit Care Med* 2008;177:433–439.
32. Verleden SE, Vasilescu DM, Willems S, Ruttens D, Vos R, Vandermeulen E, Hostens J, McDonough JE, Verbeken EK, Verschakelen J, Van Raemdonck DE, Rondelet B, Knoop C, Decramer M, Cooper J, Hogg JC, Verleden GM, Vanaudenaerde BM. The site and nature of airway obstruction after lung transplantation. *Am J Respir Crit Care Med*, 2013/12/21. 2014;189:292–300.
33. Koo HK, Vasilescu DM, Booth S, Hsieh A, Katsamenis OL, Fishbane N, Elliott WM, Kirby M, Lackie P, Sinclair I, Warner JA, Cooper JD, Coxson HO, Paré PD, Hogg JC, Hackett TL. Small airways disease in mild and moderate chronic obstructive pulmonary disease: a cross-sectional study. *Lancet Respir Med* 2018;6:591–602.
34. Seibold MA, Smith RW, Urbanek C, Groshong SD, Cosgrove GP, Brown KK, Schwarz MI, Schwartz DA, Reynolds SD. The idiopathic pulmonary fibrosis honeycomb cyst contains a mucociliary pseudostratified epithelium. *PLoS One* 2013;8:e58658.

35. Plantier L, Crestani B, Wert SE, Dehoux M, Zweytick B, Guenther A, Whitsett JA. Ectopic respiratory epithelial cell differentiation in bronchiolised distal airspaces in idiopathic pulmonary fibrosis. *Thorax* 2011;66:651–657.
36. Reyfman PA, Walter JM, Joshi N, Anekalla KR, McQuattie-Pimentel AC, Chiu S, Fernandez R, Akbarpour M, Chen CI, Ren Z, Verma R, Abdala-Valencia H, Nam K, Chi M, Han SH, Gonzalez-Gonzalez FJ, Soberanes S, Watanabe S, Williams KJN, Flozak AS, Nicholson TT, Morgan VK, Winter DR, Hinchcliff M, Hrusch CL, Guzy RD, Bonham CA, Sperling AI, Bag R, *et al.* Single-cell transcriptomic analysis of human lung provides insights into the pathobiology of pulmonary fibrosis. *Am J Respir Crit Care Med* 2019;199:1517–1536.
37. Zuo WL, Rostami MR, LeBlanc M, Kaner RJ, O’Beirne SL, Mezey JG, Leopold PL, Quast K, Visvanathan S, Fine JS, Thomas MJ, Crystal RG. Dysregulation of club cell biology in idiopathic pulmonary fibrosis. *PLoS One* 2020;15:e0237529.
38. Guha A, Vasconcelos M, Cai Y, Yoneda M, Hinds A, Qian J, Li G, Dickel L, Johnson JE, Kimura S, Guo J, McMahon J, McMahon AP, Cardoso W V. Neuroepithelial body microenvironment is a niche for a distinct subset of Clara-like precursors in the developing airways. *Proc Natl Acad Sci U S A* 2012;109:12592–12597.
39. Kotton DN, Morrissey EE. Lung regeneration: Mechanisms, applications and emerging stem cell populations. *Nat Med* 2014;20:822-832.
40. Seibold MA, Wise AL, Speer MC, Steele MP, Brown KK, Loyd JE, Fingerlin TE, Zhang W, Gudmundsson G, Groshong SD, Evans CM, Garantziotis S, Adler KB, Dickey BF, du Bois RM, Yang I V., Herron A, Kervitsky D, Talbert JL, Markin C, Park J, Crews AL,

- Slifer SH, Auerbach S, Roy MG, Lin J, Hennessy CE, Schwarz MI, Schwartz DA. A Common MUC5B Promoter Polymorphism and Pulmonary Fibrosis . *N Engl J Med* 2011;364:1503–1512.
41. Piciucchi S, Tomassetti S, Ravaglia C, Gurioli C, Gurioli C, Dubini A, Carloni A, Chilosi M, Colby T V, Poletti V. From “traction bronchiectasis” to honeycombing in idiopathic pulmonary fibrosis: A spectrum of bronchiolar remodeling also in radiology? *BMC Pulm Med* 2016;16:87.
  42. Staats P, Kligerman S, Todd N, Tavora F, Xu L, Burke A. A comparative study of honeycombing on high resolution computed tomography with histologic lung remodeling in explants with usual interstitial pneumonia. *Pathol Res Pr* 2015;211:55–61.
  43. Walsh SLF, Wells AU, Sverzellati N, Devaraj A, von der Thüsen J, Yousem SA, Colby T V., Nicholson AG, Hansell DM. Relationship between fibroblastic foci profusion and high resolution CT morphology in fibrotic lung disease. *BMC Med* 2015;13:241.
  44. Paré PD, Mitzner W. Airway-Parenchymal Interdependence. *Compr Physiol* Hoboken, NJ, USA: John Wiley & Sons, Inc.; 2012. p. 1921–1935.
  45. Coxson HO, Hogg JC, Mayo JR, Behzad H, Whittall KP, Schwartz DA, Hartley PG, Galvin JR, Wilson JS, Hunninghake GW. Quantification of idiopathic pulmonary fibrosis using computed tomography and histology. *Am J Respir Crit Care Med* 1997;155:1649–1656.
  46. Tanizawa K, Handa T, Nagai S, Hirai T, Kubo T, Oguma T, Ito I, Ito Y, Watanabe K, Aihara K, Ikezoe K, Oga T, Chin K, Izumi T, Mishima M. Clinical impact of high-attenuation and cystic areas on computed tomography in fibrotic idiopathic interstitial

- pneumonias. *BMC Pulm Med* 2015;15:74.
47. Kim HJ, Brown MS, Chong D, Gjertson DW, Lu P, Kim HJ, Coy H, Goldin JG. Comparison of the quantitative CT imaging biomarkers of idiopathic pulmonary fibrosis at baseline and early change with an interval of 7 months. *Acad Radiol* 2015;22:70–80.
  48. Ash SY, Harmouche R, Vallejo DL, Villalba JA, Ostridge K, Gunville R, Come CE, Onieva Onieva J, Ross JC, Hunninghake GM, El-Chemaly SY, Doyle TJ, Nardelli P, Sanchez-Ferrero G V, Goldberg HJ, Rosas IO, San Jose Estepar R, Washko GR. Densitometric and local histogram based analysis of computed tomography images in patients with idiopathic pulmonary fibrosis. *Respir Res* 2017;18:45.
  49. Miller ER, Putman RK, Diaz AA, Xu H, San Jose Estepar R, Araki T, Nishino M, Poli de Frias S, Hida T, Ross J, Coxson H, Dupuis J, O'Connor GT, Silverman EK, Rosas IO, Hatabu H, Washko G, Hunninghake GM. Increased Airway Wall Thickness in Interstitial Lung Abnormalities and Idiopathic Pulmonary Fibrosis. *Ann Am Thorac Soc* 2019;16:447–454.
  50. Maldonado F, Moua T, Rajagopalan S, Karwoski RA, Raghunath S, Decker PA, Hartman TE, Bartholmai BJ, Robb RA, Ryu JH. Automated quantification of radiological patterns predicts survival in idiopathic pulmonary fibrosis. *Eur Respir J* 2014;43:204–212.
  51. Ohkubo H, Nakagawa H, Niimi A. Computer-based quantitative computed tomography image analysis in idiopathic pulmonary fibrosis: A mini review. *Respir Investig* 2018;56:5–13.
  52. Jacob J, Bartholmai BJ, Rajagopalan S, Van Moorsel CHM, Van Es HW, Van Beek FT, Struik MHL, Kokosi M, Egashira R, Brun AL, Nair A, Walsh SLF, Cross G, Barnett J, De

- Lauretis A, Judge EP, Desai S, Karwoski R, Ourselin S, Renzoni E, Maher TM, Altmann A, Wells AU. Predicting outcomes in idiopathic pulmonary fibrosis using automated computed tomographic analysis. *Am J Respir Crit Care Med* 2018;198:767–776.
53. Galbán CJ, Han MK, Boes JL, Chughtai KA, Meyer CR, Johnson TD, Galbán S, Rehemtulla A, Kazerooni EA, Martinez FJ, Ross BD. Computed tomography-based biomarker provides unique signature for diagnosis of COPD phenotypes and disease progression. *Nat Med* 2012;18:1711–1715.
  54. Vasilescu DM, Martinez FJ, Marchetti N, Galbán CJ, Hatt C, Meldrum CA, Dass C, Tanabe N, Reddy RM, Lagstein A, Ross BD, Labaki WW, Murray S, Meng X, Curtis JL, Hackett TL, Kazerooni EA, Criner GJ, Hogg JC, Han MLK. Noninvasive imaging biomarker identifies small airway damage in severe chronic obstructive pulmonary disease. *Am J Respir Crit Care Med* 2019;200:575–581.
  55. Verleden SE, Kirby M, Everaerts S, Vanstapel A, McDonough JE, Verbeken EK, Braubach P, Boone MN, Aslam D, Verschakelen J, Ceulemans LJ, Neyrinck AP, Van Raemdonck DE, Vos R, Decramer M, Hackett TL, Hogg JC, Janssens W, Verleden GM, Vanaudenaerde BM. Small airway loss in the physiologically ageing lung: a cross-sectional study in unused donor lungs. *Lancet Respir Med* 2021;9:167–174.

**Table 1: Demographic and quantitative MDCT data for study subjects**

	<b>Control</b>	<b>IPF</b>
Cases, n	8	8
Age, years	60 ± 10	61 ± 5
Males/Females	7/1	5/3
Height, cm	175 ± 5	170 ± 8
Weight, kg	89 ± 14	78 ± 10
Smoking history (never/former)	4/3 <sup>†</sup>	2/6
Pack-years in former smokers	15 ± 0	28 ± 16
<b>Pulmonary function testing</b>		
FVC, L	4.29 ± 0.50 <sup>§</sup>	2.08 ± 0.62*
FEV <sub>1</sub> , L	3.33 ± 0.43 <sup>§</sup>	1.67 ± 0.50*
FEV <sub>1</sub> /FVC, %	78 ± 2 <sup>§</sup>	80 ± 8
DLCO, %predicted	N/A	33 ± 11 <sup>‡</sup>
<b>Specimen MDCT data</b>		
Total lung volume, mL	3340 (776)	1346 (799)*
Mean CT value, HU	−876 (55)	−540 (180)*
% airspace volume, %	88 (5)	57 (17)*
% tissue volume, %	12 (5)	43 (17)*

Data are shown as mean ± SD or median (interquartile range).

\*p < 0.001 vs. Controls.

<sup>§</sup>Global Lung Function Initiative-estimated values are shown.

<sup>†</sup>Smoking history in one control is unknown.

<sup>‡</sup>DLCO data in 2 patients are not available.

## Figure legends

### Figure 1: Study workflow

Pre-operative thoracic MDCT scans of patients with idiopathic pulmonary fibrosis (IPF) were used for a radiological CT diagnosis of IPF (see Table E1). Whole lung specimens (left or right lung) were inflated with air and frozen, then scanned while frozen using MDCT. Specimen CT scans were used for the quantitative analysis of lung volume, % mean attenuation and large airway morphometry. Frozen lung specimens were cut transversely into 23mm thick slices and 8 systematic uniform random (SUR) samples (23mm x 23mm) were obtained throughout the whole lung. Image registration between lung photo slices and specimen MDCT scans enabled co-localization of sample regions (red circles). All tissue samples were scanned frozen and microCT scans were used for stereological assessment of the small airway and parenchymal structures. A section of the tissue sample (4.5mm) was then formalin-fixed, paraffin-embedded, sectioned, and stained with hematoxylin and eosin for histopathological diagnosis.

### Figure 2: Comparison of large and small airway features between control and IPF lungs

Axial mid-slice computed tomography (MDCT) scans from the lungs of a representative control (A) and IPF case (B) are shown (left panels). The location of a systematic uniform random (SUR) tissue sample taken from the slices is indicated by dashed red circles. The second panel shows the reconstructed airway tree for the specimen MDCT scan from the lateral perspective. The third panel shows mid-slice microCT scans at 13µm resolution of the tissue sample circled in red. The fourth panel shows the small airway tree segmentations obtained from the microCT scans visualized in 3D. Terminal (TB, arrow-heads) and transitional (TrB, stars) bronchioles are



identified. The final panel shows a representative cross-sectional image of the terminal bronchiole highlighted by the yellow arrow-head for both the control and IPF tissue samples.

Graphs 2C – 2F show the comparison of large and small airway measurements between control and IPF lungs for whole lungs derived from the specimen MDCT scans: (C) total number of airways visible on CT, (D) number of airways by generation visible on CT, (E) airway wall area and (F) airway lumen area measured for airways in generation 7-17.

Graphs 2G-2N show parameters derived from the microCT scans: (G) shows the total number of TBs per lung, (H) the total number of TrBs per lung, (I) TB wall area, (J) coefficient of variance (CV) of TB wall thickness, (K) TB lumen area, (L) TB lumen roundness, (M) TB lumen branch roughness, and (N) TB lumen branch curviness. \* indicates p-value < 0.05, \*\* indicates p-value < 0.01 and \*\*\* indicates p-value < 0.001, † no control data for comparison.

**Figure 3: Comparison of parenchymal features between control and IPF lungs** Mid-section views from micro computed tomography (microCT) scans from four systematic uniform random (SUR) tissue samples for a representative IPF (A) and control (B) lung are shown. Graphs show the comparison of parenchymal features between controls and IPF lungs expressed as whole lung values: (C) volume fraction of tissue per parenchyma, (D) volume fraction of non-aerated parenchyma, (E) mean linear intercept, (F) alveolar surface area (m<sup>2</sup>), (G) volume fraction of alveoli, (H) volume fraction of alveolar septa, (I) volume fraction of alveolar ducts, (J) septal wall thickness. \* indicates p-value < 0.05, \*\* indicates p-value < 0.01 and \*\*\* indicates p-value < 0.001. Scale bars are 2mm.

**Figure 4: Association of traction bronchiolectasis with histopathologically and radiologically defined fibrosis**

Scatter plots show the volume fraction of tissue ( $V_v(\text{tissue/par})$ ) against (A) the number of terminal bronchioles per ml of lung and (B) the number of transitional bronchioles per ml of lung for all control (labelled green) and IPF (labelled orange) tissue samples. The dashed line indicates the upper limit for the volume fraction of tissue in control tissue samples which was used to define IPF samples without and with fibrosis. Six of the IPF patients had tissue samples with and without fibrosis, and two IPF patients had only tissue samples with fibrosis. Subsequent graphs show the comparison of control tissue samples versus IPF tissue samples without (w/o) and with tissue fibrosis on a per sample basis for: (C) the number of terminal bronchioles, (D) number of transitional bronchioles, (E) terminal bronchiolar wall area, (F) terminal bronchiolar lumen branch roughness. \* indicates  $p\text{-value} < 0.05$ , \*\* indicates  $p\text{-value} < 0.01$  and \*\*\* indicates  $p\text{-value} < 0.001$ .

Images G and H show mid-section microCT scans of an IPF tissue sample without (G) and with (H) fibrosis demonstrating the integrity of parenchymal structures in the sample without fibrosis. The vascular network is outlined in blue. Honeycomb cysts (orange arrow heads) are shown in the tissue sample with fibrosis. In I and J the same microCT images are overlaid with the 3D rendering of the small airway tree in the IPF tissue sample without fibrosis (G) and with fibrosis (H). This illustrates the distorted and dilated small airway tree forming honeycomb cysts in the IPF tissue sample with fibrosis. Scale bars are 2mm.

**Figure 5: Association between mean specimen CT attenuation values and features of traction bronchiolectasis**

The mean computed tomography (CT) attenuation value for the region on the lung specimen where the systematic uniform random (SUR) tissue samples were taken was correlated with (A) terminal bronchiole (TB) wall area ( $\text{mm}^2$ ), (B) TB lumen area ( $\text{mm}^2$ ), (C) TB lumen branch

roughness, (D) volume fraction of tissue ( $V_v(\text{tissue}/\text{par})$ ), (E) septal wall thickness ( $\mu\text{m}$ ) and (F) alveolar surface density ( $1/\text{cm}$ ). All control tissue samples are labelled green and IPF tissues samples are labelled orange. The data were assessed using a linear mixed effects model and the standardize  $\beta$  values for IPF samples are provided. A p-value  $< 0.05$  was considered significant.

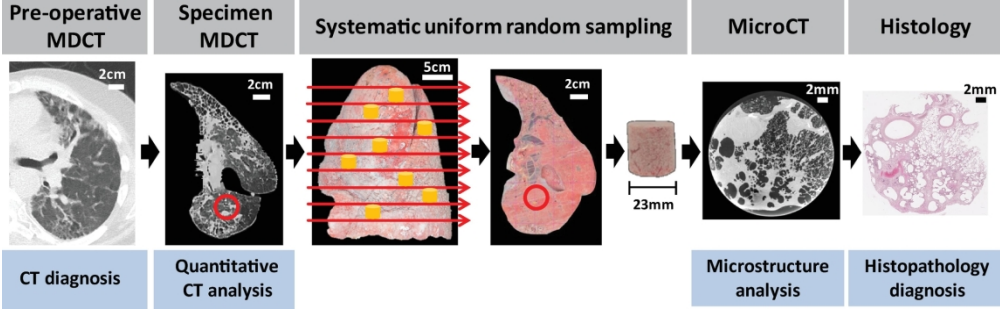


Figure 1: Pre-operative thoracic MDCT scans of patients with idiopathic pulmonary fibrosis (IPF) were used for a radiological CT diagnosis of IPF (see Table E1). Whole lung specimens (left or right lung) were inflated with air and frozen, then scanned while frozen using MDCT. Specimen CT scans were used for the quantitative analysis of lung volume, % mean attenuation and large airway morphometry. Frozen lung specimens were cut transversely into 23mm thick slices and 8 systematic uniform random (SUR) samples (23mm x 23mm) were obtained throughout the whole lung. Image registration between lung photo slices and specimen MDCT scans enabled co-localization of sample regions (red circles). All tissue samples were scanned frozen and microCT scans were used for stereological assessment of the small airway and parenchymal structures. A section of the tissue sample (4.5mm) was then formalin-fixed, paraffin-embedded, sectioned, and stained with hematoxylin and eosin for histopathological diagnosis.

202x62mm (300 x 300 DPI)

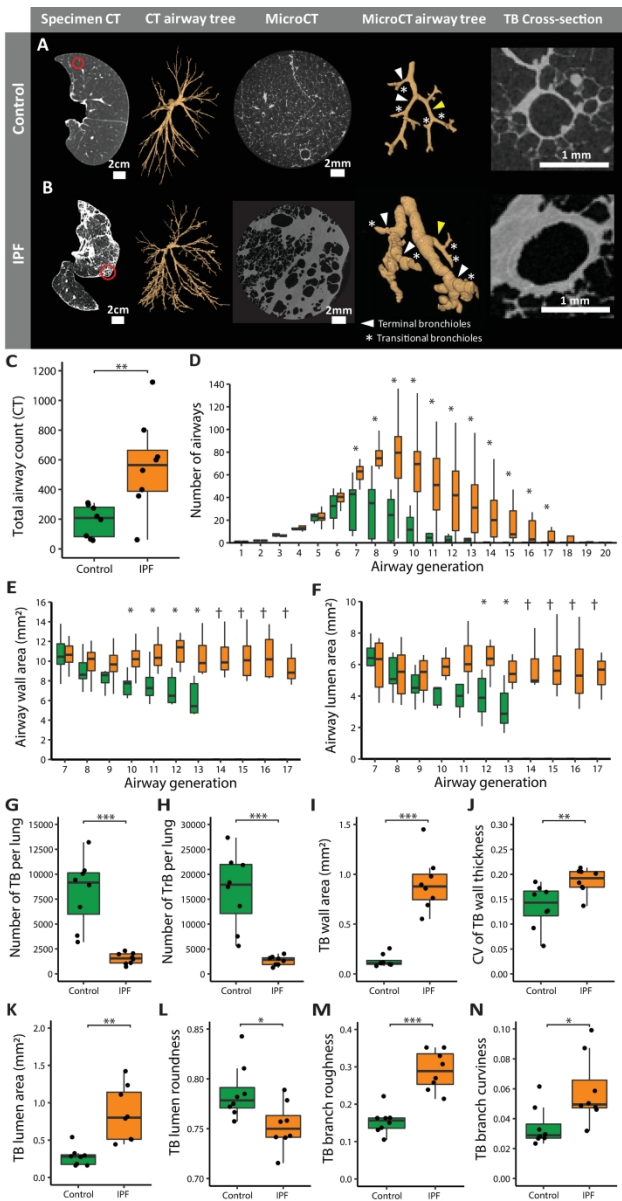


Figure 2: Axial mid-slice computed tomography (MDCT) scans from the lungs of a representative control (A) and IPF case (B) are shown (left panels). The location of a systematic uniform random (SUR) tissue sample taken from the slices is indicated by dashed red circles. The second panel shows the reconstructed airway tree for the specimen MDCT scan from the lateral perspective. The third panel shows mid-slice microCT scans at 13µm resolution of the tissue sample circled in red. The fourth panel shows the small airway tree segmentations obtained from the microCT scans visualized in 3D. Terminal (TB, arrow-heads) and transitional (TrB, stars) bronchioles are identified. The final panel shows a representative cross-sectional image of the terminal bronchiole highlighted by the yellow arrow-head for both the control and IPF tissue samples. Graphs 2C – 2F show the comparison of large and small airway measurements between control and IPF lungs for whole lungs derived from the specimen MDCT scans: (C) total number of airways visible on CT, (D) number of airways by generation visible on CT, (E) airway wall area and (F) airway lumen area measured for airways in generation 7-17. Graphs 2G-2N show parameters derived from the microCT scans: (G) shows the total number of TBs per lung, (H) the total number of TrBs per lung, (I) TB wall area, (J) coefficient of variance (CV) of TB wall thickness, (K) TB lumen area, (L) TB lumen roundness, (M) TB lumen

branch roughness, and (N) TB lumen branch curviness. \* indicates p-value < 0.05, \*\* indicates p-value < 0.01 and \*\*\* indicates p-value < 0.001, † no control data for comparison.

207x400mm (300 x 300 DPI)

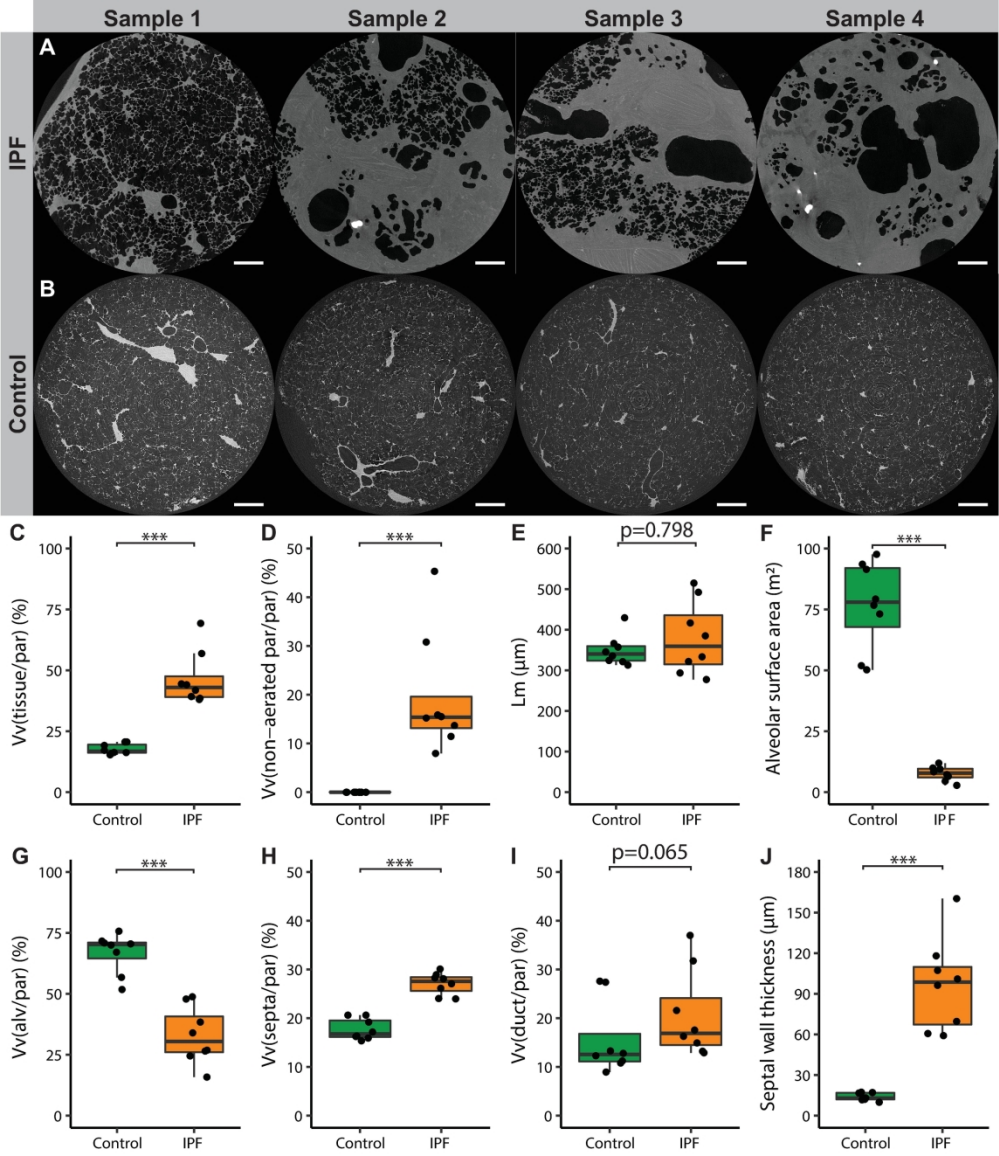


Figure 3: Mid-section views from micro computed tomography (microCT) scans from four systematic uniform random (SUR) tissue samples for a representative IPF (A) and control (B) lung are shown. Graphs show the comparison of parenchymal features between controls and IPF lungs expressed as whole lung values: (C) volume fraction of tissue per parenchyma, (D) volume fraction of non-aerated parenchyma, (E) mean linear intercept, (F) alveolar surface area (m<sup>2</sup>), (G) volume fraction of alveoli, (H) volume fraction of alveolar septa, (I) volume fraction of alveolar ducts, (J) septal wall thickness. \* indicates p-value < 0.05, \*\* indicates p-value < 0.01 and \*\*\* indicates p-value < 0.001. Scale bars are 2mm.

219x254mm (300 x 300 DPI)

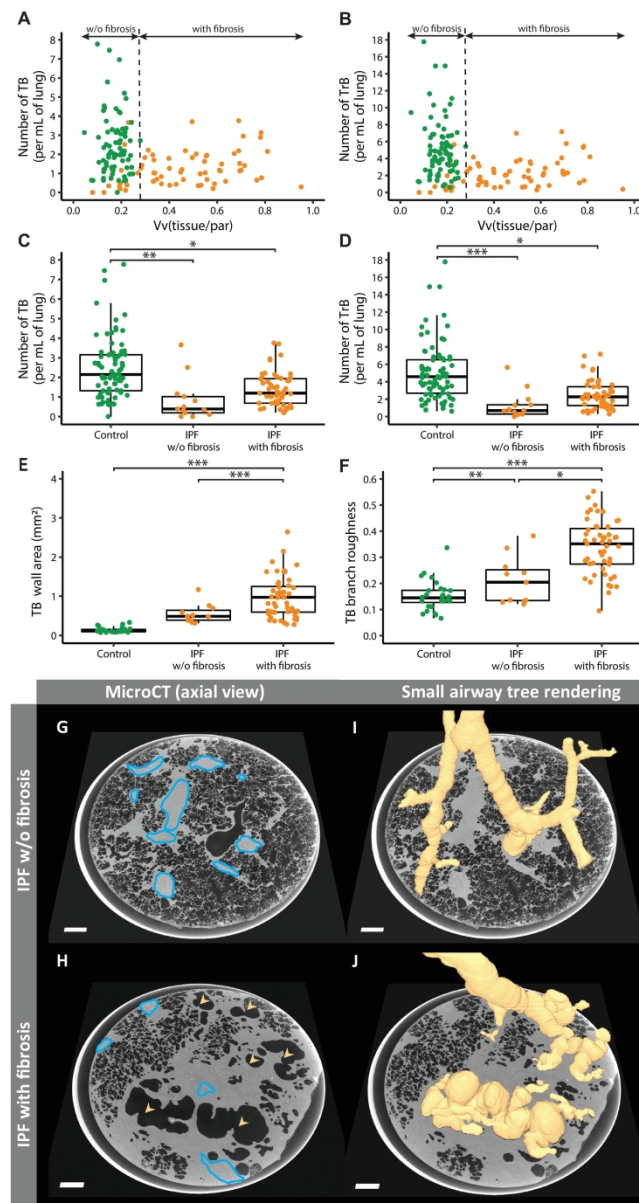


Figure 4: Scatter plots show the volume fraction of tissue (Vv(tissue/par)) against (A) the number of terminal bronchioles per ml of lung and (B) the number of transitional bronchioles per ml of lung for all control (labelled green) and IPF (labelled orange) tissue samples. The dashed line indicates the upper limit for the volume fraction of tissue in control tissue samples which was used to define IPF samples without and with fibrosis. Six of the IPF patients had tissue samples with and without fibrosis, and two IPF patients had only tissue samples with fibrosis. Subsequent graphs show the comparison of control tissue samples versus IPF tissue samples without (w/o) and with tissue fibrosis on a per sample basis for: (C) the number of terminal bronchioles, (D) number of transitional bronchioles, (E) terminal bronchiolar wall area, (F) terminal bronchiolar lumen branch roughness. \* indicates p-value < 0.05, \*\* indicates p-value < 0.01 and \*\*\* indicates p-value < 0.001. Images G and H show mid-section microCT scans of an IPF tissue sample without (G) and with (H) fibrosis demonstrating the integrity of parenchymal structures in the sample without fibrosis. The vascular network is outlined in blue. Honeycomb cysts (orange arrow heads) are shown in the tissue sample with fibrosis. In I and J the same microCT images are overlaid with the 3D rendering of the small airway tree in the IPF tissue sample without fibrosis (G) and with fibrosis (H). This illustrates the



distorted and dilated small airway tree forming honeycomb cysts in the IPF tissue sample with fibrosis. Scale bars are 2mm.

178x329mm (300 x 300 DPI)

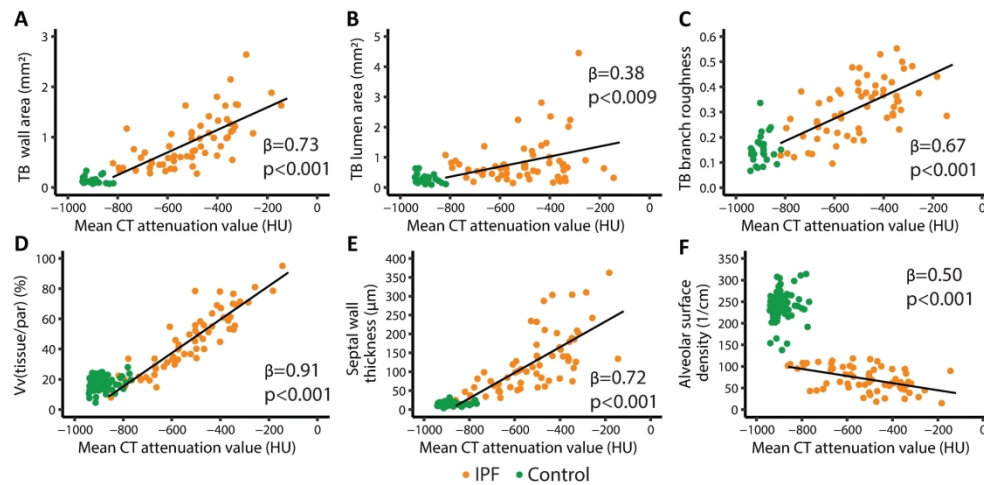


Figure 5: The mean computed tomography (CT) attenuation value for the region on the lung specimen where the systematic uniform random (SUR) tissue samples were taken was correlated with (A) terminal bronchiole (TB) wall area (mm<sup>2</sup>), (B) TB lumen area (mm<sup>2</sup>), (C) TB lumen branch roughness, (D) volume fraction of tissue (Vv(tissue/par)), (E) septal wall thickness (µm) and (F) alveolar surface density (1/cm). All control tissue samples are labelled green and IPF tissues samples are labelled orange. The data were assessed using a linear mixed effects model and the standardize  $\beta$  values for IPF samples are provided. A p-value < 0.05 was considered significant.

210x100mm (300 x 300 DPI)

## **Online Supplement:**

# **Small Airway Reduction and Fibrosis is an Early Pathologic Feature of Idiopathic Pulmonary Fibrosis**

**Running title:** Small airways disease in IPF

Kohei Ikezoe<sup>1</sup>, Tillie-Louise Hackett<sup>1</sup>, Samuel Peterson<sup>3</sup>, Dante Prins<sup>1</sup>, Cameron J. Hague<sup>2</sup>, Darra Murphy<sup>2</sup>, Stacey LeDoux<sup>1</sup>, Fanny Chu<sup>1</sup>, Feng Xu<sup>1</sup>, Joel D. Cooper<sup>5</sup>, Naoya Tanabe<sup>6</sup>, Christopher J. Ryerson<sup>1</sup>, Peter D. Paré<sup>1</sup>, Harvey O. Coxson<sup>1</sup>, Thomas V. Colby<sup>4</sup>, James C. Hogg<sup>1</sup>, and Dragoş M. Vasilescu<sup>1</sup>

<sup>1</sup>Centre for Heart and Lung Innovation, St. Paul's Hospital, University of British Columbia, Vancouver, BC, Canada,

<sup>2</sup>Department of Radiology, University of British Columbia, Vancouver, BC, Canada,

<sup>3</sup>VIDA Diagnostics, Coralville, IA, USA,

<sup>4</sup>Department of Laboratory Medicine and Pathology, Mayo Clinic, Scottsdale, AZ, USA,

<sup>5</sup>Department of Thoracic Surgery, University of Pennsylvania. Philadelphia, PA, USA,

<sup>6</sup>Department of Respiratory Medicine, Graduate School of Medicine, Kyoto University, Kyoto

**Table of contents:**

1. Table E1. Diagnostic information of IPF cases
2. Airway skeleton based measurements
  - a. Computation of airway branch length
  - b. Computation of cross-sectional images
3. Quantitative assessment of airway distortions
  - a. Roughness
  - b. Curviness
  - c. Biological interpretation of roughness and curviness
4. Stereological quantification of the lung parenchyma in IPF
5. Table E2: MicroCT analysis data per case (IPF cases)
6. Table E3 MicroCT analysis data per case (Control cases)

**Table E1. Diagnostic information of IPF cases**

Case	CT diagnosis	Histopathology diagnosis	Final clinical diagnosis
1	UIP	UIP	IPF
2	Alternative diagnosis	UIP	IPF
3	UIP	UIP	IPF
4	UIP	UIP	IPF
5	UIP	UIP	IPF
6	UIP	UIP	IPF
7	Alternative diagnosis	UIP	IPF
8	Alternative diagnosis	UIP	IPF

**Airway skeleton-based measurements**

The small airways in IPF display a high degree of distortion (Figure 5 in main manuscript) potentially caused by the tissue remodeling surrounding the airways. The distortions can be visually described as localized dilatations or constrictions leading to twisted and curved airways. To enable a quantitative assessment of these morphometric changes, it was important to develop new mathematical descriptions of these geometric attributes based on the centerline (skeleton line) of the segmented airways. After all conducting airways as well as the first generation of respiratory bronchioles were segmented, the terminal bronchioles were labeled as the last generation of conducting airways. The skeleton of the whole airway tree was calculated and 11 cross-sections perpendicular to the general direction of the terminal bronchioles were computed along the whole bronchiole branch in 10% increments. Figure E1 provides an overview of the

skeletonization processing and cross-sectional image extraction. The following sections describe the methodology for obtaining cross-sectional images and quantification of degree of distortion of the small airways.

### ***Computation of airway branch length***

A skeleton line generated from a 3D image segmentation is limited by the resolution (voxel size = pixel length \* pixel width \* pixel depth) of the original image, as represented by the white dots inside the sub-panel in Figure E1C. This means that each skeleton is a list of discrete points that are connected by lines only for visual appearance. The simple sum of all voxels that form a skeleton is not accurate due to neighboring points being joined in 2 or 3 cartesian directions.

Therefore, to calculate the correct branch length the following formula is implemented:

$$L = \sum_{i=2}^N |\vec{P}_i - \vec{P}_{i-1}| = \sum_{i=2}^N \sqrt{(x_i - x_{i-1})^2 + (y_i - y_{i-1})^2 + (z_i - z_{i-1})^2}$$

Where  $\vec{P}$  denotes the position of a voxel on the skeleton line as 3D coordinates, which are scaled based on the resolution of the scan.  $N$  indicates the total voxel count for the airway, with  $i$  denoting index number.

### ***Computation of cross-sectional images***

Obtaining cross-sectional images in airways from normal subjects or patients with COPD is relatively simple since their airways are generally very straight. However, as visualized in this manuscript, the distortion of airways in IPF patients is highly significant and previous methods of obtaining true cross-sections was not applicable. Therefore, the algorithms for determining branch length and the correct angle of cross-sections had to be revised to address highly distorted airways.

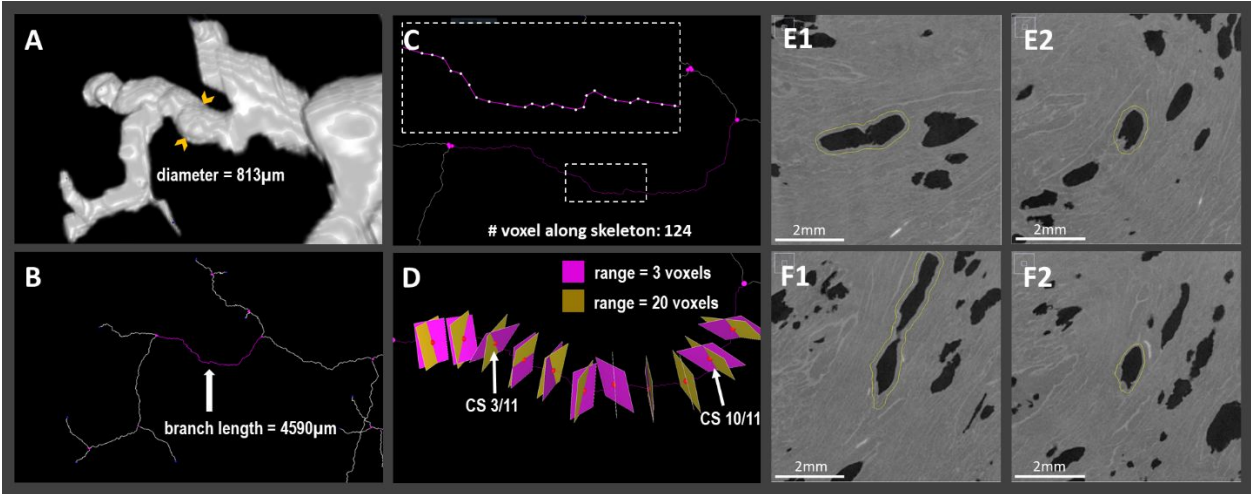


**Figure E1: The process of obtaining cross-sectional images:** (A): A 3D rendering of an airway segmentation generated from the MicroCT scan. (B) One airway branch in the skeleton tree generated from the airways visualized in A is selected (magenta color) and the calculated branch length is shown below. (C) A closer view of the skeleton with annotated voxels (white dots) showing the mathematical basis for the skeleton where a line is interpolated between the points for visual purposes, (D) A 3D depiction of the alignment of cross sections generated from the image, the parameter range concerns the calculation direction for such cross sections, (E) A pair of cross section images generated at the point marked *CS 3/11* in D with the parameter range set to 3 and 20, E1 and E2 respectively. (F) A pair of cross section images generated at the point marked *CS 10/11* in D with the parameter range set to 3 and 20, F1 and F2 respectively.

The goal of cross-sectional image analysis is to obtain true measurements of wall and lumen areas. To minimize the effect of oblique cuts through an airway which would increase wall thicknesses and provide the wrong impression of the airway shape, it is crucial to calculate the correct cross-sectional plane through an airway. Small, localized distortions of the airway skeleton line can lead to the computation of the wrong cross-sectional plane if only a small number of skeleton line points are used.

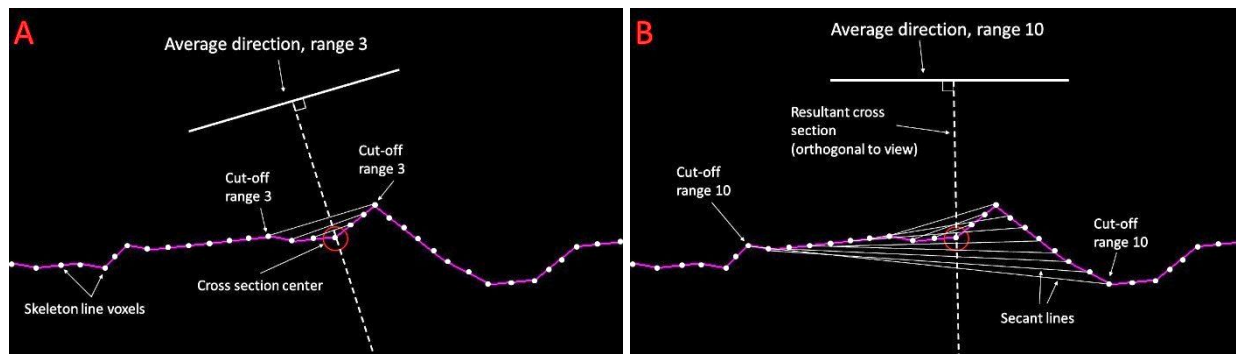


**Figure E2: Example of calculation of cross-section plane based on secant line averaging:** A magnified portion of a skeleton line (purple) represents 1mm of a whole airway branch and is used as an example. Small “bumps” in the skeleton line are caused by noise related imperfections in the airway segmentation and should not be allowed to affect measurements. The discrete skeleton line voxels are depicted by dots (white), with secant lines (white lines) being drawn between the same number of voxels to the left and right of the voxel (circled in red) for which the cross-section should be calculated. (A) Shows the average direction calculated from 3 secant lines. (B) Shows the average direction calculated from 10 secant lines. Resulting cross-section plane (dashed line) is shown in both sub-panels (A and B) for the respective number of secant lines used, highlighting the impact of choosing an appropriate number of points.

A formula was developed from the principle that a cross-section is orthogonal to the path of an airway. Thus, to find the cross-section of a continuous multivariable function a tangent line at the desired point should be used, indicating the instantaneous direction of the skeleton line at that location. A visualization of normal planes based on 3D tangent lines can be performed on the online platform GeoGebra (1). Because of the discrete nature of the skeleton line, a more robust method must be used to find an approximate tangent line. The most immediate solution is the secant line (a straight line intersecting two points on a function) between the two neighboring voxels. However, because of the noise associated with operating at the resolution limit of the microCT scan and the forced discreteness of voxel points of the raw images, it is important to compute the final tangent based on an average of multiple secant lines, as illustrated in Figure E2.

Given a vector  $\vec{P}_n$ , representing the position of the voxel at which we wish to generate a cross section, secant lines are drawn between neighbors from this center voxel at increasing integers



from 1 to the desired range R, i.e. 20. These secant lines can be seen in Figure E2 as white lines between voxels indicated as dots. The average direction of these secant lines is then calculated as  $\vec{V}$  which represents the direction of the skeleton line at the cross-section center seen for two ranges (6 and 20 points) as shown in Figures E2A and E2B.

$$\vec{V} = \sum_{i=1}^R (\vec{P}_{n-i} - \vec{P}_{n+i}) = \sum_{i=1}^R \langle x_{n-i} - x_{n+i} \mid y_{n-i} - y_{n+i} \mid z_{n-i} - z_{n+i} \rangle$$

Where  $\vec{P}_n$  is a vector representing the 3D position of the central voxel for the cross section, and n is its index. R is the consideration range, the maximum # of voxels to be considered. For airways with a length of <200 voxels, the range of the first and last cross-section will be reduced up to the maximum value possible value given the limits of the voxel count.  $\vec{V}$  is a vector that describes the direction of the airway which the orthogonal cross-section plane is then calculated. Using the direction of  $\vec{V}$ , the angle to rotate the original CT image can be procedurally calculated which we center at  $\vec{P}_0$  after the transformation producing the final cross-sectional images.

The value of the consideration range R must be carefully selected (not too large or too small) so that the calculation of the orthogonal plane is not susceptible to minor local inaccuracies, but still accounting for airway curves. To determine a pertinent value of R, manual inspection of the cross-sectional images along with 3D visualizations of the tangent lines were done. From the 3D cross section alignment indicated by colored squares in Figure E1D, a range of R=20 produces cross-sections with a more accurate alignment to the airway's path. In particular, CS3/11 in Figure E1D corresponds to the cross-sections in Figure E1E and CS10/11 to Figure E1F. It was found that a consideration range of 20 in both directions, R=20 gave the more accurate results as shown in Figure E1E2 and E1F2 compared to Figure E1E1 and E1F1 for which a value of R=3

was used. Using a range exceeding 20 was found to reduce the sensitivity to curves in the airway that were flattened out by the long consideration range. In comparison a range less than 20 was found to be susceptible to small variance and noise present at the limits of the image's resolution, as seen in the comparison between a shorter and longer range in Figure E2A and E2B, where the overall curve of the airway is better captured in Figure E2B.

### Quantitative assessment of airway distortions

The most commonly used metric for evaluating the degree of distortion of a line or a tube such as an airway branch is called tortuosity (2). An equation for tortuosity typically used is  $T = \frac{L_p}{L_c}$  where  $L_p$  is the length of a path (airway skeleton line) and  $L_c$  is the straight line between the start and end point (branch points in an airway tree), denoted  $c$  for chord length. An example of this calculation is given in Figure E3A. Tortuosity must always be greater than 1 and depends on the amount of curving and also distortion or “roughness” of the path. However, tortuosity alone cannot be used to differentiate between a path with many small distortions (i.e. rough) and a curved path because it is dependent on both roughness and curviness as depicted in Figure E3B. Therefore, a new formula was constructed that takes tortuosity into account, but accounts for the roughness attribute.

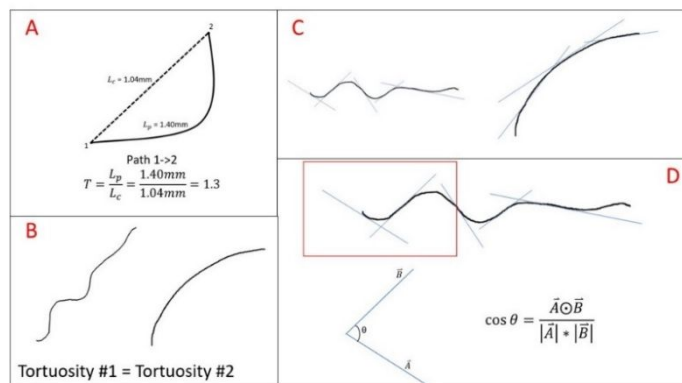


**Figure E3: Visual examples for calculating tortuosity and roughness** (skeleton line are depicted in black). (A) Tortuosity calculation for theoretical example of a curved airway path. (B) Example of two skeleton lines with the same tortuosity. (C) Examples of localized trendlines depicted in blue, are used to calculate curviness. (D) A graphical depiction of the dot product formula and its use to compare two

neighboring trendlines  $\vec{A}$  and  $\vec{B}$  to calculate roughness.

## ***Roughness***

Roughness is a parameter that can measure rapid, local changes, through the analysis of the direction of neighboring tangents along the airway center line. For straight or slowly curving airways, the direction of the tangent line changes slowly in comparison to jagged, rough airway paths where the tangent change direction rapidly. Because of the discrete nature of the voxels in each skeleton line, the tangent line was replaced with a localized trendline for a small number of voxels ( $n=7$ , empirically determined based on variation in 20 unbiasedly selected airways). A diagram of these trendlines is given in Figure E3C to show how the rough airway on the left has rapidly changing trendlines in comparison to the smooth, curving airway on the right. These trendlines are then compared to the neighboring trendlines to the left and right using the dot product formula to determine the cosine of the angle between the two, as depicted in Figure E3D with the two neighboring trendlines  $\vec{A}$  and  $\vec{B}$ .

The formula for  $\cos \theta$  is  $\cos \theta = \frac{\vec{A} \odot \vec{B}}{|\vec{A}| * |\vec{B}|}$ , where  $\vec{A} \odot \vec{B}$  is the dot product between two vectors, defined as coordinate multiplication  $\vec{A} \odot \vec{B} = x_a * x_b + y_a * y_b + z_a * z_b$  and the length of a vector  $|\vec{V}|$  is  $|\vec{V}| = \sqrt{x_v^2 + y_v^2 + z_v^2}$ . After obtaining the cosine value, the average for each of the comparisons between neighbors is computed and an empirically determined exponent of 7 is added to accentuate sensitivity. The final formula used to calculate the amount of localized distortions (roughness) of each airway branch was:

$$roughness = 1 - mean[(\cos \theta)^7] = 1 - \frac{\sum_{i=1}^{N-1} (\cos \theta)^7}{N-1} = 1 - \frac{\sum_{i=1}^{N-1} \left( \frac{\vec{T}_i \odot \vec{T}_{i+1}}{|\vec{T}_i| * |\vec{T}_{i+1}|} \right)^7}{N-1}$$

Where  $N$  is the number of trendlines,  $i$  is the current trendline index and  $\vec{T}_i$  is direction of the current trendline.

Based on the examples of potential angles between neighboring trendlines presented in Figure E4, the value of roughness can range between 0 for straight paths to 1 for paths that change direction in a right angle.

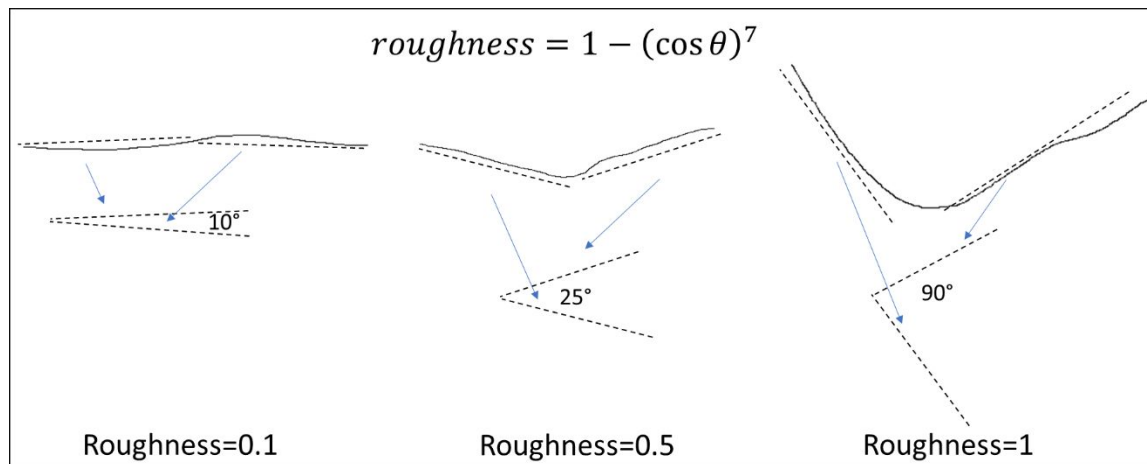


**Figure E4: Roughness measures for different angles of neighboring trendlines:** Example of different roughness values for different skeleton lines (solid lines) shown in two dimensions. Neighboring trendlines are computed and re-drawn side-by-side to illustrate roughness calculation.

### *Curviness*

As stated above, tortuosity can be used to quantify the straightness of a path which we named “**curviness**”. However, tortuosity is affected by small direction changes of a path which are quantified by our measure of roughness. By subtracting the impact of roughness from the calculated tortuosity of an airway path, we remain with a value for just the gradual and permanent curviness of an airway:

$$C = T - f(R)$$

Where C is curviness, T is tortuosity, R is roughness and f is an unknown function of roughness. This equation still has two unknowns: C and  $f(R)$ , so a data fit cannot be easily performed. To overcome this, we must determine values of C and  $f(R)$  from experimental data. The simplest method it to set C to 0, meaning zero curviness. This corresponds to macroscopically straight airway, such as the ones presented in Figure E6A. The formula then becomes:

$$T = f(R)$$

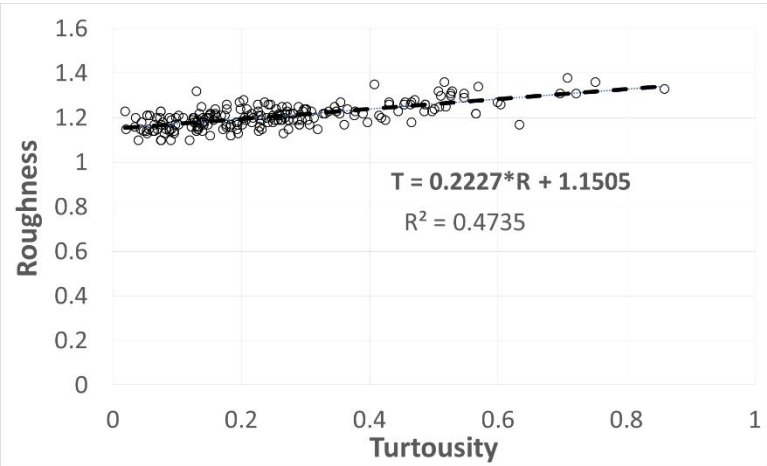


**Figure E5: Correlation between tortuosity and roughness of straight airways:** The linear regression equation for the relationship between tortuosity and roughness can be used to nullify the effects of roughness on Tortuosity. Data was taken from 202 straight airways collected from 22 tissue samples with varying degrees of roughness (higher roughness corresponding to a larger number of fine bumps).

As shown in Figure E5, data from 202 completely straight airways from a sample of 22 tissue samples was used to determine  $f(R)$  based in a linear fit. The linear regression formula of the data was used in our formula for curviness:

$$C = T - f(R)$$

$$C = T - 1.15 - 0.223 * R$$

This equation can describe the curviness of all airways using information from the data for only straight airways, as the purpose of the fit was to nullify the effects of roughness on tortuosity.

Theoretically, a straight airway path would have a calculated Tortuosity of 1, which should result in a curviness of 0. However, based on the constant in the new formula of 1.15, the curviness for a perfectly straight “theoretical” airway would be -0.15. The additional -0.15 in the constant is due to small pixel based “bumps” of the skeleton caused by the discrete nature of voxels at the pixel limit of images. Figure E6(A-D) provides examples of different skeleton lines from airways with different degrees of roughness and curviness. The fine zig-zagging of the skeleton lines at the pixel level leads our data to the possibility of minor negative values for curviness as shown in Figure E6B. Such values can be attributed to imperfections in the image resolution, which have not been found to tangibly skew data.

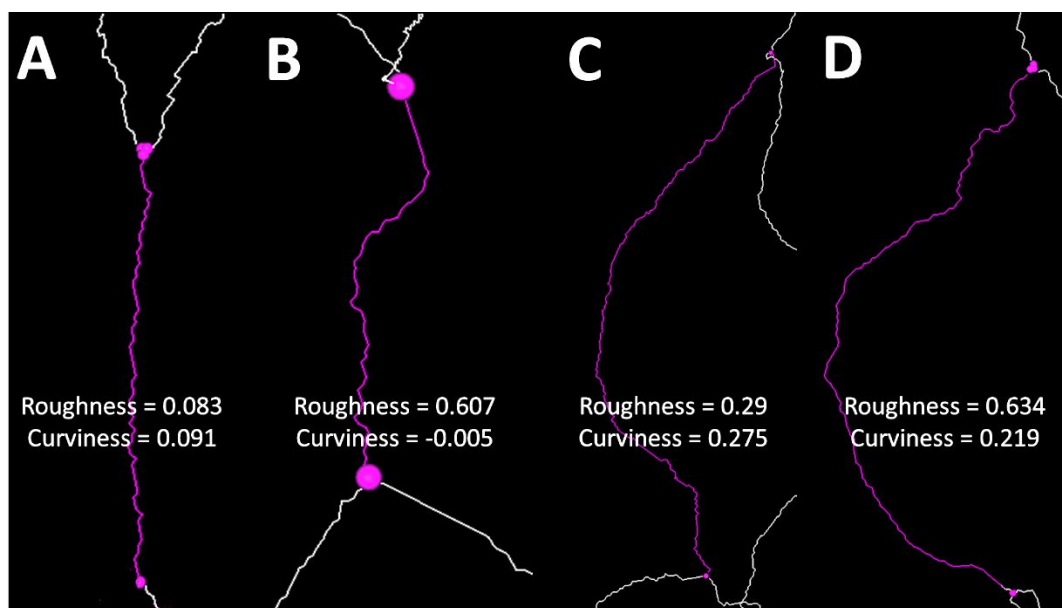
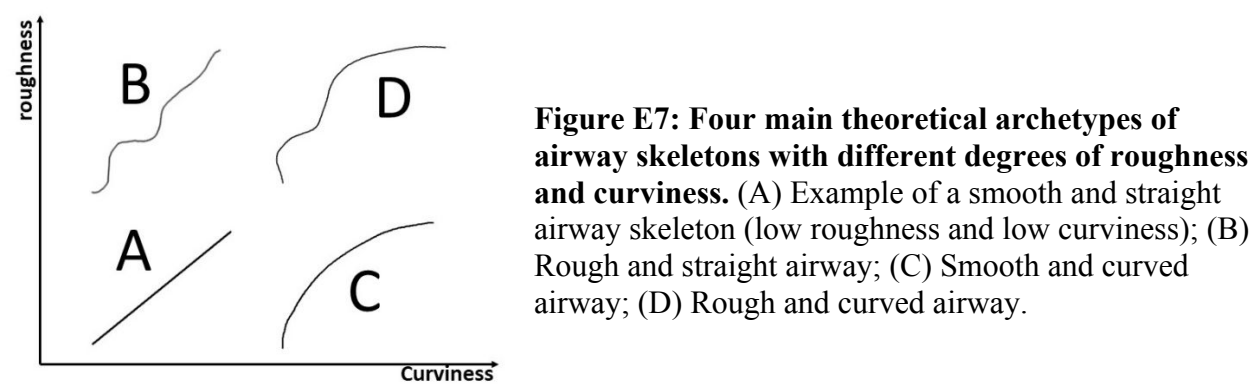


**Figure E6: Examples of the four distinct types of airways:** The four types of individual airway skeleton lines depicted here correspond to the four theoretical ‘archetypes’ from Figure E7. Magenta dots indicate branch points. The roughness and curviness values for each analyzed airway path (magenta) are shown in white text. (A) Example of a straight smooth airway (low roughness and curviness); (B) Example of a straight rough airway because of the central bump but overall straightness; (C) Example of a curved smooth airway (low roughness and a long continuous curve); (D) Example of a curved rough airway (high roughness and high curviness).

***Biological interpretation of roughness and curviness***

The goal of roughness and curviness is to calculate geometric attributes of airways using the skeleton line. Curviness relates to how curved the path of an airway is, excluding small distortions of the airway path which are described by the roughness. An airway can be idealized to have a high or low quality of both of these attributes and an example is given in Figure E7 that describes the four unique ‘archetype’ airways.



**Stereological quantification of the lung parenchyma in IPF**

Fibrosis, inflammation, edema and atelectasis in the IPF lung leads to impairment of gas exchange. To enable an objective differentiation of parenchyma that still contributes to gas exchange and parenchyma that is not aerated due to extensive remodeling, we followed a recently proposed classification of the parenchyma into two main groups: aerated and non-aerated(3). The diagram in Figure E8 shows the general parenchymal sub-types. This classification was used for the stereology based point counting described by Figure E9. The line intercept and point counts were used to calculate the lung structure measurements by sample and by subject using previously published formulas(3, 4).

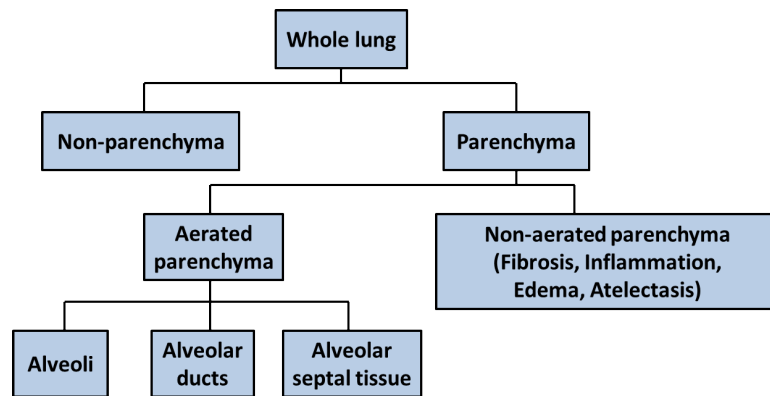


**Figure E8:** Diagram of the stratification implemented for differentiating lung parenchyma subtypes for the stereological assessment at the microCT level.

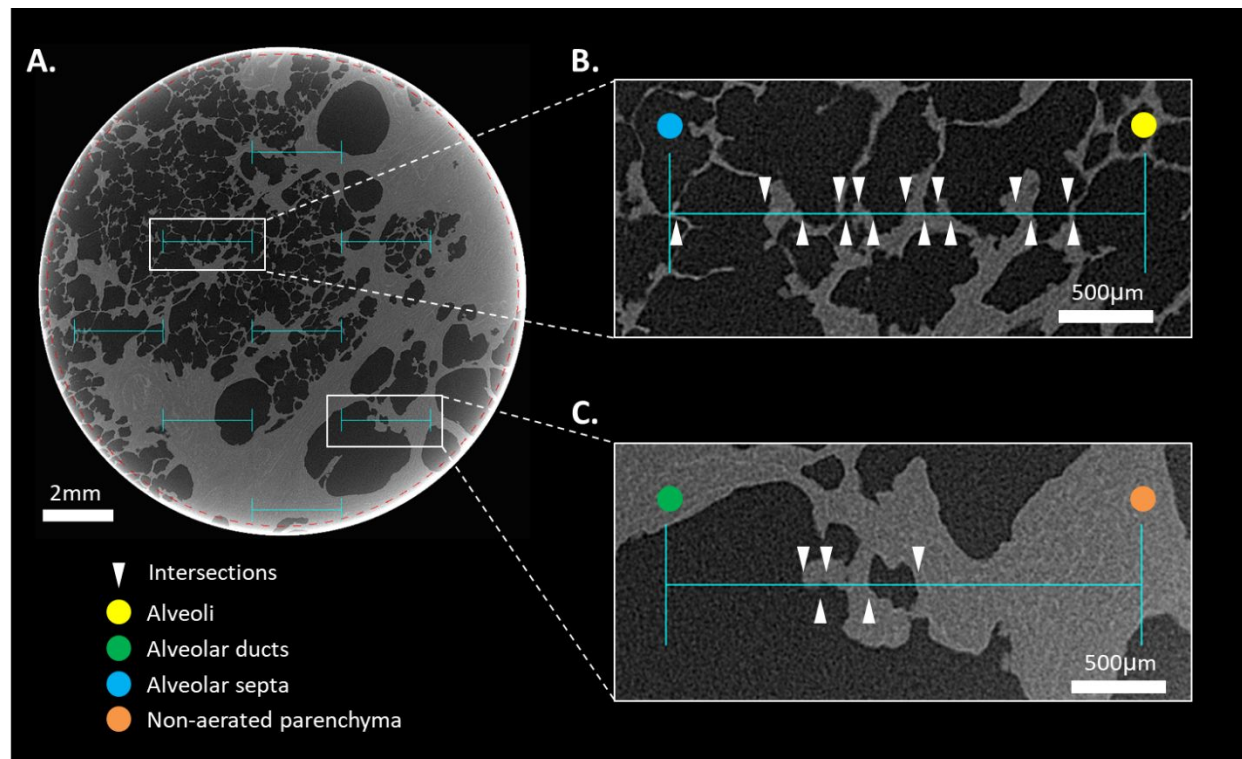


**Figure E9: Stereological counting probes applied to microCT image**

(A) Example microCT images from an IPF sample is shown with a checkered-pattern line-grid (line length of 2.5 mm) that was randomly overlaid on all images using a custom software developed in the lab. Scale bar is 2mm. (B) and (C) The line intercepts are counted and end points are highlighted depending on the type of parenchymal feature the end-point falls on. A legend of the color-coding is provided in the figure. Scale bars are 500µm.



Table E2: MicroCT analysis data per case (IPF cases)

IPF Case	1	2	3	4	5	6	7	8	Mean $\pm$ SD
<b>Lung side</b>	L	L	L	L	L	L	L	L	<b>8L</b>
<b>Age , years</b>	63	63	65	56	52	63	64	60	<b>61 <math>\pm</math> 5</b>
<b>Pack-years</b>	0	0	30	35	45	40	20	0.3	<b>21 <math>\pm</math> 19</b>
<b>Total lung volume, ml</b>	840	895	1733	1571	1641	957	1837	1121	<b>1324 <math>\pm</math> 411</b>
<b>Lm , <math>\mu</math>m</b>	277	321	515	492	333	416	385	293	<b>379 <math>\pm</math> 89</b>
<b>Alveolar surface density, 1/cm</b>	96	78	55	55	89	54	68	96	<b>74 <math>\pm</math> 18</b>
<b>Alveolar surface area, m<sup>2</sup></b>	6.5	4.5	8.4	7.2	11.9	2.8	10.0	9.5	<b>7.6 <math>\pm</math> 3.0</b>
<b>Vv(alv/par), %</b>	38.3	26.8	24.5	26.5	47.9	15.8	34.0	48.7	<b>32.8 <math>\pm</math> 11.6</b>
<b>Vv(duct/par), %</b>	17.6	16.3	37.0	31.7	12.9	14.9	21.6	13.2	<b>20.6 <math>\pm</math> 9.0</b>
<b>Vv(septa/par), %</b>	28.3	26.1	27.1	28.1	24.0	23.9	28.9	30.1	<b>27.1 <math>\pm</math> 2.2</b>
<b>Vv(non-aerated par/par), %</b>	15.8	30.8	11.4	13.7	15.2	45.3	15.5	8.0	<b>19.5 <math>\pm</math> 12.4</b>
<b>Vv(tissue/par), %</b>	44.1	56.9	38.5	41.8	39.3	69.3	44.4	38.0	<b>46.5 <math>\pm</math> 11.0</b>
<b>Septal wall thickness, <math>\mu</math>m</b>	70	96	107	118	59	160	101	61	<b>97 <math>\pm</math> 34</b>
<b>TB per lung</b>	1470	1645	1023	2056	1109	726	1985	2325	<b>1542 <math>\pm</math> 562</b>
<b>TrB per lung</b>	2616	3055	1887	3399	1895	1273	3187	4055	<b>2671 <math>\pm</math> 928</b>
<b>TB branch length, mm</b>	2.96	3.02	2.91	2.49	3.66	3.19	3.26	2.54	<b>3.00 <math>\pm</math> 0.38</b>
<b>TB lumen area, mm<sup>2</sup></b>	1.24	0.81	0.51	0.51	1.42	0.44	1.11	0.79	<b>0.85 <math>\pm</math> 0.37</b>
<b>TB lumen diameter, mm</b>	1.06	0.95	0.74	0.77	1.25	0.64	1.15	0.98	<b>0.94 <math>\pm</math> 0.21</b>
<b>TB lumen circularity</b>	0.94	0.91	0.90	0.94	0.93	0.88	0.91	0.92	<b>0.92 <math>\pm</math> 0.02</b>
<b>TB lumen roundness</b>	0.78	0.76	0.74	0.79	0.76	0.74	0.72	0.74	<b>0.75 <math>\pm</math> 0.02</b>
<b>TB wall area, mm<sup>2</sup></b>	0.86	1.06	0.76	0.69	0.90	1.45	0.98	0.55	<b>0.91 <math>\pm</math> 0.27</b>
<b>TB wall thickness, <math>\mu</math>m</b>	224	340	311	246	217	529	264	178	<b>289 <math>\pm</math> 110</b>
<b>TB CV of wall thickness</b>	0.18	0.21	0.17	0.21	0.17	0.21	0.20	0.14	<b>0.19 <math>\pm</math> 0.03</b>
<b>TB branch roughness</b>	0.33	0.26	0.24	0.27	0.35	0.35	0.21	0.31	<b>0.29 <math>\pm</math> 0.05</b>
<b>TB branch curviness</b>	0.099	0.050	0.032	0.046	0.087	0.059	0.048	0.049	<b>0.059 <math>\pm</math> 0.023</b>

Table E3 MicroCT analysis data per case (Control cases)

Control Case	1	2	3	4	5	6	7	8	Mean $\pm$ SD
<b>Lung side</b>	R	R	L	R	R	R	R	L	<b>6R 2L</b>
<b>Age, years</b>	56	64	53	77	61	64	65	42	<b>60 <math>\pm</math> 10</b>
<b>Pack-years</b>	0	15	0	0	0	NA	15	15	<b>6 <math>\pm</math> 19</b>
<b>Total lung volume, ml</b>	2313	4080	3701	2968	3611	3281	3131	3401	<b>3310 <math>\pm</math> 533</b>
<b>Lm, <math>\mu</math>m</b>	325	357	346	313	335	430	366	321	<b>349 <math>\pm</math> 37</b>
<b>Alveolar surface density, 1/cm</b>	247	269	278	307	239	186	262	299	<b>261 <math>\pm</math> 38</b>
<b>Alveolar surface area, m<sup>2</sup></b>	50.2	97.6	93.6	79.2	76.7	51.9	73.1	91.4	<b>76.7 <math>\pm</math> 18.0</b>
<b>Vv(alv/par), %</b>	51.8	70.5	70.9	75.7	67.1	56.7	71.6	70.0	<b>66.8 <math>\pm</math> 8.2</b>
<b>Vv(duct/par), %</b>	27.6	13.3	12.8	9.0	12.3	27.4	11.2	10.8	<b>15.5 <math>\pm</math> 7.5</b>
<b>Vv(septa/par), %</b>	20.6	16.2	16.3	15.3	20.6	15.9	17.2	19.2	<b>17.7 <math>\pm</math> 2.2</b>
<b>Vv(non-aerated par/par), %</b>	0.0	0.0	0.0	0.0	0.0	0.0	0.0	0.0	<b>0.0 <math>\pm</math> 0.0</b>
<b>Vv(tissue/par), %</b>	20.6	16.2	16.3	15.3	20.6	15.9	17.2	19.2	<b>17.7 <math>\pm</math> 2.2</b>
<b>Septal wall thickness, <math>\mu</math>m</b>	17	12	12	10	17	17	13	13	<b>14 <math>\pm</math> 3</b>
<b>TB per lung</b>	3833	8907	6709	10057	9428	3191	10372	13203	<b>8212 <math>\pm</math> 3414</b>
<b>TrB per lung</b>	7534	18355	13634	22308	17466	5637	21847	27363	<b>16768 <math>\pm</math> 7471</b>
<b>TB branch length, mm</b>	2.42	2.23	2.53	1.46	2.48	3.71	2.14	2.20	<b>2.40 <math>\pm</math> 0.63</b>
<b>TB lumen area, mm<sup>2</sup></b>	0.32	0.29	0.27	0.16	0.18	0.54	0.16	0.28	<b>0.28 <math>\pm</math> 0.12</b>
<b>TB lumen diameter, mm</b>	0.65	0.62	0.59	0.46	0.48	0.84	0.45	0.61	<b>0.59 <math>\pm</math> 0.13</b>
<b>TB lumen circularity</b>	0.92	0.96	0.94	0.95	0.95	0.94	0.96	0.96	<b>0.95 <math>\pm</math> 0.01</b>
<b>TB lumen roundness</b>	0.76	0.81	0.77	0.78	0.78	0.77	0.77	0.84	<b>0.79 <math>\pm</math> 0.03</b>
<b>TB wall area, mm<sup>2</sup></b>	0.20	0.09	0.11	0.08	0.11	0.26	0.11	0.10	<b>0.13 <math>\pm</math> 0.06</b>
<b>TB wall thickness, <math>\mu</math>m</b>	88	50	41	56	55	74	52	53	<b>59 <math>\pm</math> 15</b>
<b>TB CV of wall thickness</b>	0.13	0.06	0.18	0.17	0.16	0.16	0.09	0.12	<b>0.14 <math>\pm</math> 0.04</b>
<b>TB branch roughness</b>	0.22	0.15	0.13	0.16	0.10	0.16	0.14	0.16	<b>0.15 <math>\pm</math> 0.04</b>
<b>TB branch curviness</b>	0.027	0.027	0.030	0.047	0.028	0.023	0.062	0.033	<b>0.035 <math>\pm</math> 0.013</b>

## References:

1. Alberca AS. Tangent line and normal plane to a trajectory in the space – GeoGebra. *Date Accessed 2021-02-19* at <<https://www.geogebra.org/m/Q2C7EfBn>>.
2. Jones MD, Long J. Tortuosity as a metric for evaluating branch motion paths under dynamic loading. *Proc - 2012 IEEE 4th Int Symp Plant Growth Model Simulation, Vis Appl PMA 2012* 2012. p. 172–179.doi:10.1109/PMA.2012.6524830.
3. Lutz D, Gazdhar A, Lopez-Rodriguez E, Ruppert C, Mahavadi P, Günther A, Klepetko W, Bates JH, Smith B, Geiser T, Ochs M, Knudsen L. Alveolar derecruitment and collapse induration as crucial mechanisms in lung injury and fibrosis. *Am J Respir Cell Mol Biol* 2015;52:232–243.
4. Vasilescu DM, Phillion AB, Kinose D, Verleden SE, Vanaudenaerde BM, Verleden GM, Van Raemdonck D, Stevenson CS, Hague CJ, Han MK, Cooper JD, Hackett TL, Hogg JC. Comprehensive stereological assessment of the human lung using multiresolution computed tomography. *J Appl Physiol* 2020;128:1604–1616.